TOI-220b: a warm sub-Neptune discovered by TESS

Citation for the original published paper (version of record):
Hoyer, S., Gandolfi, D., Armstrong, D. et al (2021). TOI-220b: a warm sub-Neptune discovered by TESS. Monthly Notices of the Royal Astronomical Society, 505(3): 3361-3379.
http://dx.doi.org/10.1093/mnras/stab1427

Monthly Notices of the ROYAL ASTRONOMICAL SOCIETY

MNRAS **505,** 3361–3379 (2021) https://doi.org/10.1093/mnras/stab1427
Advance Access publication 2021 May 22

TOI-220 *b*: a warm sub-Neptune discovered by *TESS*

S. Hoyer [1]★ D. Gandolfi [2] D. J. Armstrong [3,4] M. Deleuil,[1] L. Acuña,[1] J. R. de Medeiros,[5] E. Goffo,[2] J. Lillo-Box,[6] E. Delgado Mena,[7,8] T. A. Lopez [1] A. Santerne [1] S. Sousa,[7,8] M. Fridlund [9,10] V. Adibekyan,[7,8] K. A. Collins,[11] L. M. Serrano [2] P. Cortés-Zuleta,[1] S. B. Howell,[12] H. Deeg [13,14] A. Aguichine,[1] O. Barragán [15] E. M. Bryant,[3,4] B. L. Canto Martins,[5] K. I. Collins,[16] B. F. Cooke [3,4] R. F. Díaz,[17] M. Esposito,[18] E. Furlan,[19] S. Hojjatpanah,[7,8] J. Jackman [3,4] J. M. Jenkins,[12] E. L. N. Jensen,[20] D. W. Latham,[9] I. C. Leão,[5] R. A. Matson [21] L. D. Nielsen [22] A. Osborn [3,4] J. F. Otegi,[22,23] F. Rodler,[24] S. Sabotta [18] N. J. Scott,[12] S. Seager,[25,26,27] C. Stockdale,[28] P. A. Strøm [3,4] R. Vanderspek,[25] V. Van Eylen [29] P. J. Wheatley [3,4] J. N. Winn,[30] J. M. Almenara [31] D. Barrado,[6] S. C. C. Barros,[7,8] D. Bayliss [3,4] F. Bouchy,[22] P. T. Boyd,[32] J. Cabrera,[33] W. D. Cochran,[34] O. Demangeon,[7,8] J. P. Doty,[35] X. Dumusque,[22] P. Figueira,[7,24] W. Fong,[25] S. Grziwa,[36] A. P. Hatzes,[18] P. Kabáth,[37] E. Knudstrup [38] J. Korth [36] J. H. Livingston [39] R. Luque [13,14] O. Mousis,[1] S. E. Mullally,[40] H. P. Osborn [25,41] E. Pallé,[13,14] C. M. Persson,[10] S. Redfield [42] N. C. Santos,[7,8] J. Smith,[12,43] J. Šubjak,[37] J. D. Twicken,[12,43] S. Udry[22] and D. A. Yahalomi[11,44]

Affiliations are listed at the end of the paper

Accepted 2021 May 4. Received 2021 May 4; in original form 2020 October 20

ABSTRACT

In this paper, we report the discovery of TOI-220 *b*, a new sub-Neptune detected by the *Transiting Exoplanet Survey Satellite* (*TESS*) and confirmed by radial velocity follow-up observations with the HARPS spectrograph. Based on the combined analysis of *TESS* transit photometry and high precision radial velocity measurements, we estimate a planetary mass of $13.8 \pm 1.0\,M_{\oplus}$ and radius of $3.03 \pm 0.15\,R_{\oplus}$, implying a bulk density of $2.73 \pm 0.47\,g\,cm^{-3}$. TOI-220 *b* orbits a relative bright ($V = 10.4$) and old (10.1 ± 1.4 Gyr) K dwarf star with a period of ∼10.69 d. Thus, TOI-220 *b* is a new warm sub-Neptune with very precise mass and radius determinations. A Bayesian analysis of the TOI-220 *b* internal structure indicates that due to the strong irradiation it receives, the low density of this planet could be explained with a steam atmosphere in radiative–convective equilibrium and a supercritical water layer on top of a differentiated interior made of a silicate mantle and a small iron core.

Key words: techniques: photometric – techniques: radial velocities – planets and satellites: fundamental parameters – planets and satellites: individual: TYC 8897-01263-1 – stars: fundamental parameters.

1 INTRODUCTION

Launched in 2018 April, the *Transiting Exoplanet Survey Satellite* (*TESS*) space mission (Ricker et al. 2015) has discovered about 98 confirmed new exoplanets and more than 2450 candidates.[1] Among all the confirmed exoplanets, one class of particular interest are the small-sized planets ($R < 5\,R_{\oplus}$) orbiting bright stars ($V < 11$ mag) with periods shorter than 10 d. Within this parameter space there is the so-called Neptunian desert (Szabó & Kiss 2011; Mazeh, Holczer & Faigler 2016), which is a region that presents a significant paucity of hot/highly irradiated planets with respect to the overall planet population. This deficit could be seen as evidence of photoevaporation and/or tidal disruptions (Owen & Lai 2018) or of core-powered atmospheric mass-loss mechanism (Ginzburg, Schlichting & Sari 2018; Gupta & Schlichting 2019). Currently, of all the known planets in the Neptunian desert only a very small number have precisely measured masses (e.g. West et al. 2019; Armstrong et al. 2020; Jenkins et al. 2020), preventing a comprehensive understanding of the formation history of these objects. On the other side, there is a population of sub-Neptune size planets exposed to a milder stellar irradiation that usually present a gas-rich envelope with equilibrium temperatures below 1000 K (e.g. Morley et al. 2015; Crossfield & Kreidberg 2017; Gao et al. 2020). In this paper, we present the discovery and confirmation of TOI-220 *b*, a sub-Neptune orbiting TYC 8897-01263-1, an old (10.1 Gyr) K0 V high proper motion southern star with a magnitude of 9.69 in the *TESS* bandpass ($V = 10.47$). Table 1 shows a summary of IDs, magnitudes and sky coordinates of TOI-220. The brightness of the star, therefore, enabled a precise high SNR radial velocity (RV) follow-up campaign with the

★ E-mail: sergio.hoyer@lam.fr

[1] Source: NASA Exoplanet Archive (Akeson et al. 2013), as of 2021 January 20.

Table 1. TOI-220 main IDs, celestial coordinates, and magnitudes.

Parameter	Value	Reference
TIC	150098860	(1)
TOI	220	(2)
TYC	8897-01263-1	(1)
APASS	29859752	(3)
2MASS	J06071197-6159487	(4)
WISE	J060711.93-615949.5	(5)
Gaia DR2	5481210874877547904	(6)
RA (J2000)	06:07:11.967	(1)
DEC (J2000)	−61:59:48.895	(1)
μ_{RA} (mas yr^{-1})	− 17.815 ± 0.046	(6)
μ_{DEC} (mas yr^{-1})	− 68.361 ± 0.042	(6)
Band	**Value**	**Reference**
TESS	9.688 ± 0.006	(1)
Johnson-*V*	10.416 ± 0.263	(3)
Johnson-*B*	11.152 ± 0.032	(3)
2MASS-*J*	9.030 ± 0.024	(4)
2MASS-*H*	8.631 ± 0.031	(4)
2MASS-*Ks*	8.542 ± 0.025	(4)
WISE-W1	8.476 ± 0.023	(5)
WISE-W2	8.525 ± 0.020	(5)
WISE-W3	8.381 ± 0.021	(5)
WISE-W4	8.526 ± 0.167	(5)
Gaia G	10.1897 ± 0.003	(6)
Gaia B_p	10.6078 ± 0.0012	(6)
Gaia R_p	9.6408 ± 0.0007	(6)

Notes. (1) TIC v8 (Stassun et al. 2019).
(2) TOI Catalogue (Guerrero et al. 2021).
(3) AAVSO Photometric All-Sky Survey (Henden et al. 2015).
(4) Two Micron All Sky survey (Skrutskie et al. 2006).
(5) AllWISE Catalogue (Cutri et al. 2014).
(6) *Gaia* DR2 (Gaia Collaboration 2018).

High Accuracy Radial velocity Planet Searcher (HARPS; Pepe et al. 2002) spectrograph mounted at the ESO La Silla 3.6 m telescope, in the framework of the NCORES (e.g. Armstrong et al. 2020; Nielsen et al. 2020) and KESPRINT (e.g. Gandolfi et al. 2018; Carleo et al. 2020) collaborations. The confirmation of the planetary nature of TOI-220 *b* is based on the simultaneous analysis of the *TESS* photometry and HARPS RV measurements.

The rest of the paper is organized as follows. The gathered observations of the TOI-220 system are described in Section 2. The stellar analysis, the combined modelling, and the timing analysis of the transits are presented in Section 3. In Section 4, we describe the Bayesian analysis of the internal structure of TOI-220 *b* and the final discussion is presented in Section 5.

2 OBSERVATIONS

2.1 *TESS* observations

During *TESS* Southern ecliptic hemisphere observations, TOI-220 was observed through sectors 1–12 with the exception of sector 3. By the end of the writing of this work, the sectors 27 and 28 light curves were released, as part of the *TESS* extended survey in the Southern hemisphere. These data were included in the timing analysis (Section 3.4) and in the search for transits of the hypothetical planet *c* (Appendix C). The transit signals of TOI-220.01 (aka TOI-220 *b*) were detected by the *TESS* Science Processing Operations Center (SPOC; Jenkins et al. 2016) transit search pipeline (Jenkins 2002; Jenkins et al. 2010; Li et al. 2019). The transit detection threshold crossing event, with a periodicity of 10.695 d, a depth of ∼900 ppm, and an SNR ∼ 28, subsequently passed all SPOC data validation diagnostic tests (Twicken et al. 2018) and was promoted to *TESS* Object of Interest (TOI) status as a planet candidate (Guerrero et al. 2021). For each *TESS* sector, the light curve of the target was retrieved from the Mikulski Archive for Space Telescopes (MAST) archive. In this work, the two-minute cadence Pre-search Data Conditioning Simple Aperture Photometry (PDCSAP) light curves (Smith et al. 2012; Stumpe et al. 2012, 2014) detrended with the SPOC algorithms were used. Two or three transits of TOI-220 *b* were identified using a simple Box Least Squares (BLS) analysis on per-Sector light curves. After a first inspection of the flux time-series of each sector some transits of TOI-220 *b* were discarded due to SNR considerations and/or due to large systematics in the flux time-series. This was the case for the full light curve of Sector 11. A few transits with poor coverage (incomplete transits) were also discarded. Therefore, only one or two transits per *TESS* Sector were finally extracted. A total of 17 out of the 24 transits of TOI-220 *b* observed by *TESS* were considered for further analysis. After a first estimation of the individual time of transits using the period obtained from the BLS analysis, we extracted the photometric light curves around 0.4 d before/after the transit central time, when possible. The *TESS* sector, central time, and the 2 min RMS of each transit used in this work are reported in Table 2 and the light curves are shown in Fig. 1.

Table 2. Summary of TOI-220 *b* transits extracted from the *TESS* data.

TESS Sector	Transit mid-time [BJD_TDB]	RMS (2 min) (ppm)
S01	2458335.9024	890
S01	2458346.5976	941
S02	2458357.2928	897
S02	2458378.6832	903
S04	2458421.4640	979
S04	2458432.1592	909
S05	2458442.8544	942
S05	2458453.5496	949
S06	2458474.9400	952
S06	2458485.6352	882
S07	2458496.3304	908
S07	2458507.0257	929
S08	2458528.4161	924
S09	2458549.8065	911
S10	2458592.5873	833
S12	2458635.3681	961
S12	2458646.0633	938

2.2 HARPS follow-up

We obtained radial velocity measurements of TOI-220 with the HARPS spectrograph (Mayor et al. 2003) mounted on the 3.6 m telescope at ESO's La Silla Observatory. HARPS is a stabilized high-resolution spectrograph with resolving power of $R \approx 115\,000$, capable of sub m s^{-1} RV precision. In total 101 observations were taken between 2018 November 18 and 2019 October 11 in high accuracy mode, of which 91 were used in the combined fit. Observations were performed under programmes 1102.C-0923 (PI: Gandolfi), 1102.C-0249 (PI: Armstrong), 0102.C-0584 (PI: De Medeiros), 60.A-9700, and 60.A-9709 (technical time). A typical exposure time of 1800 s

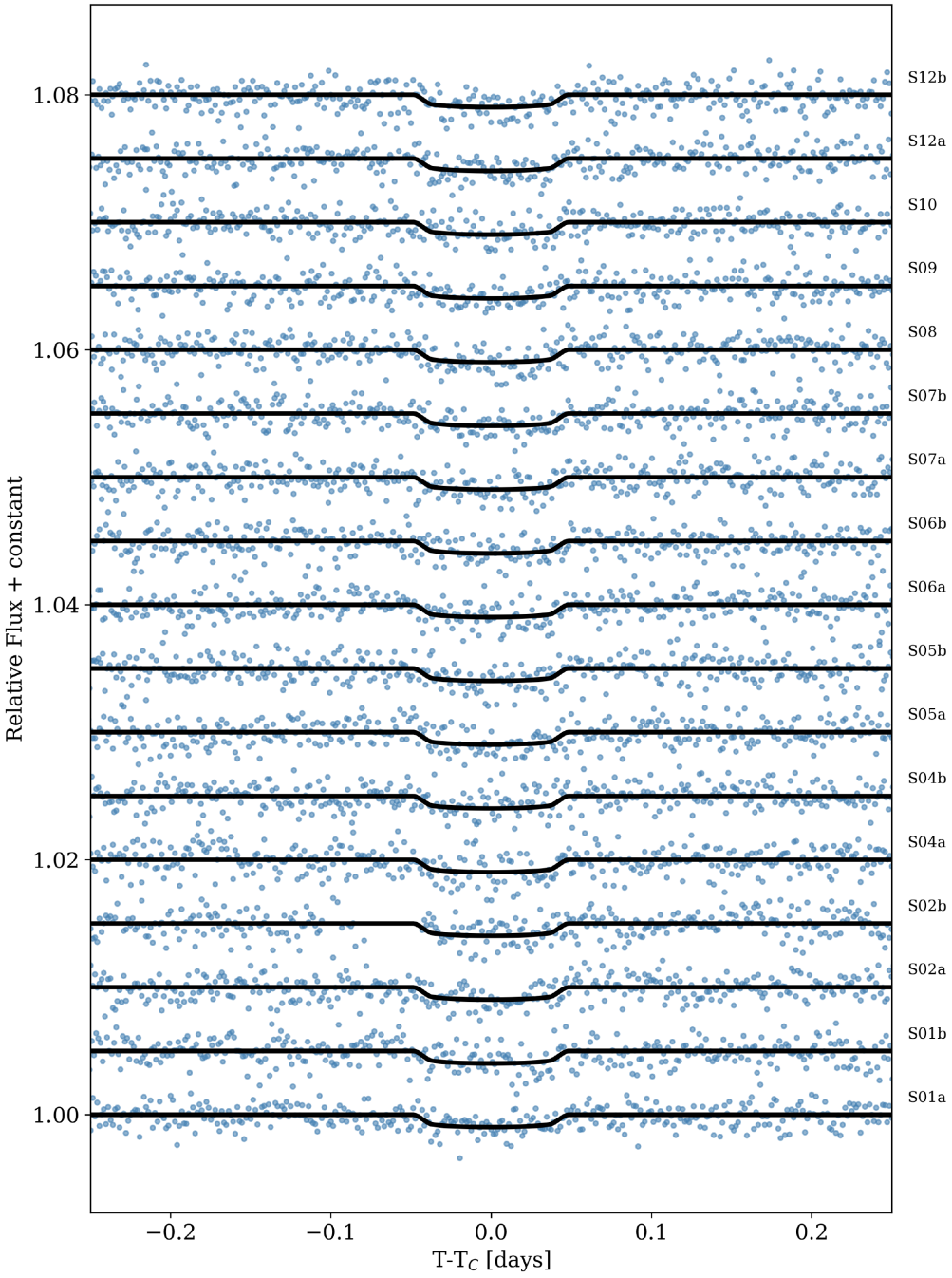

Figure 1. TOI-220 *b* transit light curves extracted from the *TESS* data. The black solid line represents the best transit model (Section 3.3). The labels indicate the corresponding *TESS* sector.

was used, on occasion adjusted between 1500 s and 2100 s depending on sky condition and observing schedule. We achieved a typical signal-to-noise per pixel of 60 and an RV precision of 1.0 m s^{-1}.

Eight observations acquired on the nights between 2018 November 25 and 27 were excluded. On these dates the ThAr lamp used for wavelength calibration of HARPS was deteriorating and was subsequently exchanged on 2018 November 28. The changing flux ratio between the thorium and argon emission lines of the dying ThAr lamp induced a 2 m s^{-1} d^{-1} drift in the wavelength solution of the instrument over 5 d. The problematic data were confirmed by comparing unpublished data from the HARPS-N solar telescope (Dumusque et al. 2015; Collier Cameron et al. 2019) and those of the Helios program on HARPS, which also observes the Sun daily. Another observation done on the night of the 2019 January 19 was excluded due to an earthquake on that night.[2] Finally, one observation on the night of the 2019 April 17 was excluded due to its very low signal-to-noise ratio. This gives 91 useful spectra.

The data were reduced with the HARPS data reduction software (DRS; Lovis & Pepe 2007). Radial velocity measurements were derived using the weighted cross-correlation function (CCF)

[2]https://www.volcanodiscovery.com/earthquakes/2019/01/20/01h32/magnitude7-NearCoastofCentralChile-quake.html.

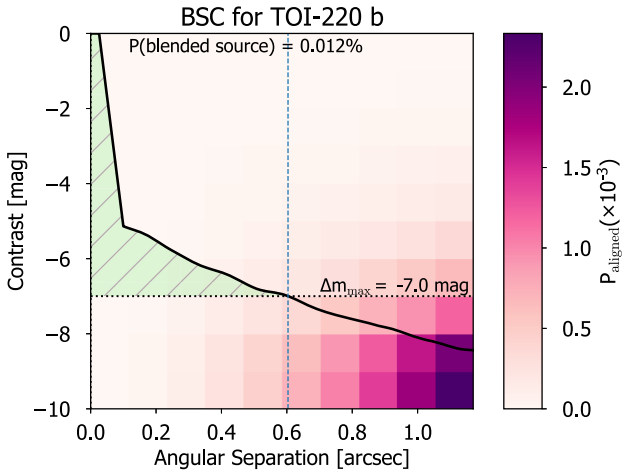

Figure 2. Contrast curve from the Gemini/Zorro instrument for the 832 nm filter (solid black line). The colour on each angular separation and contrast bin represents the probability of a chance-aligned source with these properties at the location of the target, based on TRILEGAL model (see Section 2.3 within the main text). The maximum contrast of a blended binary capable of mimicking the planet transit depth is shown as a dotted horizontal line. The green-shaded region represents the non-explored regime by the high-spatial resolution image. The BSC corresponds to the integration of $P_{\rm aligned}$ over this shaded region.

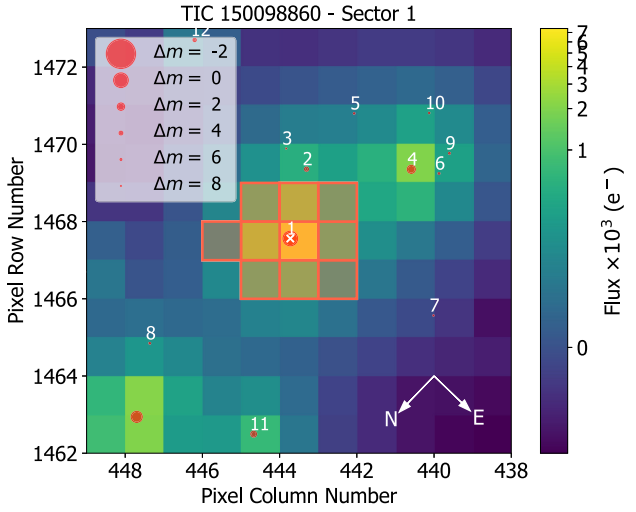

Figure 3. Target Pixel File of the *TESS* frame for TOI-220 corresponding to Sector 1 and computed with TPFPLOTTER (Aller et al. 2020). The SPOC pipeline aperture is highlighted as red squares and the Gaia DR2 catalogue is over plotted with symbol sizes proportional to the magnitude contrast with the target.

method using a K0 numerical mask (Pepe et al. 2002). For each spectrum, the DRS provides also the contrast, the full-width at half maximum (FWHM), and the bisector inverse slope (BIS) of the cross-correlation function, as well as the Ca II H & K lines activity indicator (log R'_{HK}). We also extracted additional activity indexes and spectral diagnostics, namely, Hα, Na D, chromaticity (CRX), and differential line width (dLW), using the code SERVAL (Zechmeister et al. 2018). The 91 DRS and SERVAL RV measurements and activity indicators are listed in Tables G1 and G2. Time stamps are given in Barycentric Julian Dates in Barycentric Dynamical Time (BJD_TDB). The RV time-series along with the best-fitting model are described in Section 3.3. We found an RV jitter below 2 m s^{-1}, consistent with the low activity level of the star (see Sections 3.1 and 3.3).

2.3 High-resolution imaging

To search for contaminating stars in the *TESS* photometric aperture, TOI-220 was observed on 2020 January 9 with the Zorro speckle instrument at Gemini South telescope.[3] Zorro provides simultaneous speckle imaging in two bands, 562 and 832 nm, with output data products including a reconstructed image, and robust limits on companion detections (Howell et al. 2011). The contrast curve for the 832 nm is shown in Fig. 2. We also calculated from our high-resolution images the probability of contamination from blended and undetectable sources in the *TESS* aperture. We call this the blended source confidence (BSC) and the steps for estimating this probability are fully described in Lillo-Box, Barrado & Bouy (2014). We used a PYTHON implementation of this technique (BSC, by J. Lillo-Box) which uses the TRILEGAL[4] Galactic model (version 1.6; Girardi et al. 2012) to retrieve a simulated source population of the region around the corresponding target.[5] From this simulated population, the density of stars around the target position (radius $r = 1^\circ$) was derived with the associated probability of chance-alignment at a given contrast magnitude and separation. We used the default parameters for the bulge, halo, thin/thick discs, and the lognormal initial mass function from Chabrier (2001). The Zorro contrast curve was then used to constrain this parameter space and estimate the final probability of undetected potentially contaminant sources. We considered as potentially contaminant sources those with a maximum contrast magnitude of $\Delta m_{\rm max} = -2.5 \log \delta$, with δ being the transit depth of the candidate planet in the *TESS* band. This represents the maximum magnitude that a blended star can have to mimic this transit depth. We converted the depth in the *TESS* passband to the Zorro filters by using simple conversions using the TIC catalogue magnitudes and linking the 562 nm filter to the SDSSr band and the 832 nm filter to the SDSSz band. The corresponding conversions imply $\Delta m_{562\,\rm nm} = 0.954 \Delta m_{\rm TESS}$ and $\Delta m_{832\,\rm nm} = 0.920 \Delta m_{\rm TESS}$.

We applied this technique to TOI-220 using the two contrast curves available from the Gemini/Zorro instrument. The result provides a very low probability for an undetected source capable of mimicking the transit signal of 0.055 per cent for the 562 nm image and 0.015 per cent for the 832 nm image. We underline that using high-resolution images allowed us to significantly improve these probabilities by 26 per cent and 81 per cent for the 562 and 832 nm images, respectively, when comparing to the raw probabilities (i.e. without high-resolution images). As an example, we show in Fig. 2 the contrast curve and the results of the BSC analysis. In addition, by using the TPFPLOTTER code (Aller et al. 2020) we ruled out the presence of contaminant sources within the *TESS* photometric aperture down to a Δmag = 8 mag in the Gaia DR2 catalogue (see Fig. 3).

[3] https://www.gemini.edu/sciops/instruments/alopeke-zorro/.
[4] http://stev.oapd.inaf.it/cgi-bin/trilegal.

[5] This is done in PYTHON by using the ASTROBASE implementation by Bhatti et al. (2020).

2.4 Ground based photometric follow-up

We observed transit ingresses of TOI-220 *b* in Pan-STARRS *z*-short band on 2019 February 13 and 2019 December 21 from the LCOGT (Brown et al. 2013) 1.0 m network node at South Africa Astronomical Observatory. We used the TESS TRANSIT FINDER, which is a customized version of the TAPIR software package (Jensen 2013), to schedule our transit observations. The 4096 × 4096 LCOGT SINISTRO cameras have an image scale of 0.389 arcsec per pixel, resulting in a 26 × 26 arcmin field of view. The images were calibrated by the standard LCOGT BANZAI pipeline, and photometric data were extracted with AstroImageJ (Collins et al. 2017). The 2019 February 13 images were focused and have typical stellar point-spread-functions with an FWHM of 1.″9, and circular apertures with radius 4.″3 were used to extract the differential photometry. The 2019 December 21 images were defocused and have typical stellar point-spread-functions with an FWHM of 5.″2, and circular apertures with radius 7.″8 were used to extract the differential photometry. The light curves are presented in Appendix F1.

3 DATA ANALYSIS

3.1 Stellar parameters

We derived the spectroscopic parameters and chemical abundance of TOI-220 from the co-added spectrum, which has an S/N per pixel at 5500 Å of ∼600. We used ARES+MOOG and followed the methodology described in Santos et al. (2013) and Sousa (2014) to derive the stellar atmospheric parameters ($T_{\rm eff}$, log *g*, microturbulence, [Fe/H]), and their respective uncertainties. We first measured equivalent widths (EW) of iron lines on the combined HARPS spectrum of TOI-220 using the ARES v2 code[6] (Sousa et al. 2015). Then we used a minimization process where we assume ionization and excitation equilibrium to converge in the best set of spectroscopic parameters. This process makes use of a grid of Kurucz model atmospheres (Kurucz 1993) and the radiative transfer code MOOG (Sneden 1973). Stellar abundances of the elements were derived using the classical curve-of-growth analysis method assuming local thermodynamic equilibrium (e.g. Adibekyan et al. 2012, 2015; Delgado Mena et al. 2014, 2017). Abundances of the volatile elements, C and O, were derived following the method of Delgado Mena et al. (2010), Bertran de Lis et al. (2015). Since the two analysed spectral lines of oxygen (6158.17 and 6300.3 Å) are usually weak and the 6300.3 Å line is blended with a Ni line (see e.g. Bertran de Lis et al. 2015), the EWs of these lines were manually measured with the task SPLOT in IRAF. All the [X/H] ratios are obtained by doing a differential analysis with respect to a high S/N solar spectrum from HARPS, obtained from archival observations of the asteroid Vesta.

The stellar parameters and abundances of the elements are presented in Table 3. These results are in agreement with the values obtained from the Bayesian analysis described in Section 3.3. We found that the [X/Fe] ratios of α elements are slightly above solar. This fact together with a metallicity of −0.22 dex indicate that TOI-220 is probably an old star from the thin disc (e.g. Delgado Mena et al. 2019). Moreover, we used the chemical abundances of some elements to derive ages through the so-called chemical clocks (i.e. certain chemical abundance ratios which have a strong correlation for age). We applied the 3D formulas described in table 10 of Delgado Mena et al. (2019), which also consider the variation in age produced by the effective temperature and iron abundance. We used the chemical clocks [Y/Mg], [Y/Zn], [Y/Ti], [Y/Si], [Y/Al], [Sr/Ti], [Sr/Mg], and [Sr/Si] from which we obtain a weighted average age of 10.1 ± 1.4 Gyr. This age is in agreement (within their uncertainties) with the age obtained from the Bayesian analysis described in the Section 3.3.

Following Johnson & Soderblom (1987), we calculated the space velocity components (UVW) with respect to the local standard of rest, adopting the standard solar motion ($U_\odot$, $V_\odot$, $W_\odot$) = (11.1, 12.24, 7.25) km s^{-1} of Schönrich, Binney & Dehnen (2010). Then, following Bensby, Feltzing & Lundström (2003) we calculated the probability of the star belonging to different stellar populations. For more details about the calculations of the kinematic properties of the stars (see Adibekyan et al. 2012). Our calculations suggest that TOI-220 belongs to the Galactic thin disc with a 98 per cent probability, in agreement with the chemical classification.

Finally, Canto Martins et al. (2020) studied TOI-220 in their recent study of 1000 TOIs and found no evidence of a coherent rotation period in the photometry, indicative of a low activity level. With a mean value of the Ca II H & K lines activity index of $\log R'_{\rm HK} = -5.07 \pm 0.05$, TOI-220 is magnetically less active than the Sun whose $\log R'_{\rm HK}$ ranges from −4.86 to −4.95 from solar maximum to minimum (Hall, Lockwood & Skiff 2007).

3.2 Periodogram analysis of the HARPS measurements

We performed a frequency analysis of the HARPS RVs and spectral diagnostics to search for the Doppler reflex motion induced by TOI-220 *b* and unveil the presence of additional signals that might be associated to stellar activity and/or arise from the orbital motion of other planets in the system.

The generalized Lomb–Scargle (GLS) periodogram (Zechmeister & Kürster 2009) of the HARPS DRS RVs (Fig. 4, upper panel) shows a significant peak at $f_{\rm b} = 0.093$ d^{-1}, i.e. the orbital frequency of the transiting planet detected in the *TESS* light curve. We estimated its false-alarm probability (FAP) using the bootstrap method described in Murdoch, Hearnshaw & Clark (1993). Briefly, we computed the periodogram of 10^6 mock time-series obtained by shuffling the RV measurements and their uncertainties, while keeping the time-stamps fixed. We defined the FAP as the fraction of those periodograms whose highest power exceeds the observed power of $f_{\rm b}$ in the periodogram of the original HARPS data at any frequency. We found no false positives out of our 10^6 trials, implying that $f_{\rm b}$ has an FAP $< 10^{-6}$. Moreover, the peak at $f_{\rm b}$ does not appear in any of the periodograms of the activity indicators[7] (Fig. 4), confirming that the Doppler signal is induced by the presence of a bona fide planet, namely, TOI-220 *b*.

We subtracted the Doppler signal of the transiting planet TOI-220 b from the HARPS RVs by fitting a circular model, fixing the period and T_0 to the values derived from the modelling of the *TESS* light curves (with T_0 being equal to the mid-time of the first *TESS* transit), while allowing for the systemic velocity and RV semi-amplitude to vary. The GLS periodogram of the RV residuals displays significant (FAP < 0.1 per cent) power at frequencies lower than ∼0.008 d^{-1} (125 d), with a peak at about 0.0032 d^{-1} (309 d) (Fig. 4, second panel). Despite this peak being undetected in the periodograms of the activity indicators and line asymmetry diagnostics (Fig. 4) – suggesting the presence of an additional outer companion – we note

[6]The ARES v2 code can be downloaded at http://www.astro.up.pt/~sousasag/ares.

[7]For the CCF's FWHM and BIS we arbitrarily adopted uncertainties twice as large as those of the RV measurements.

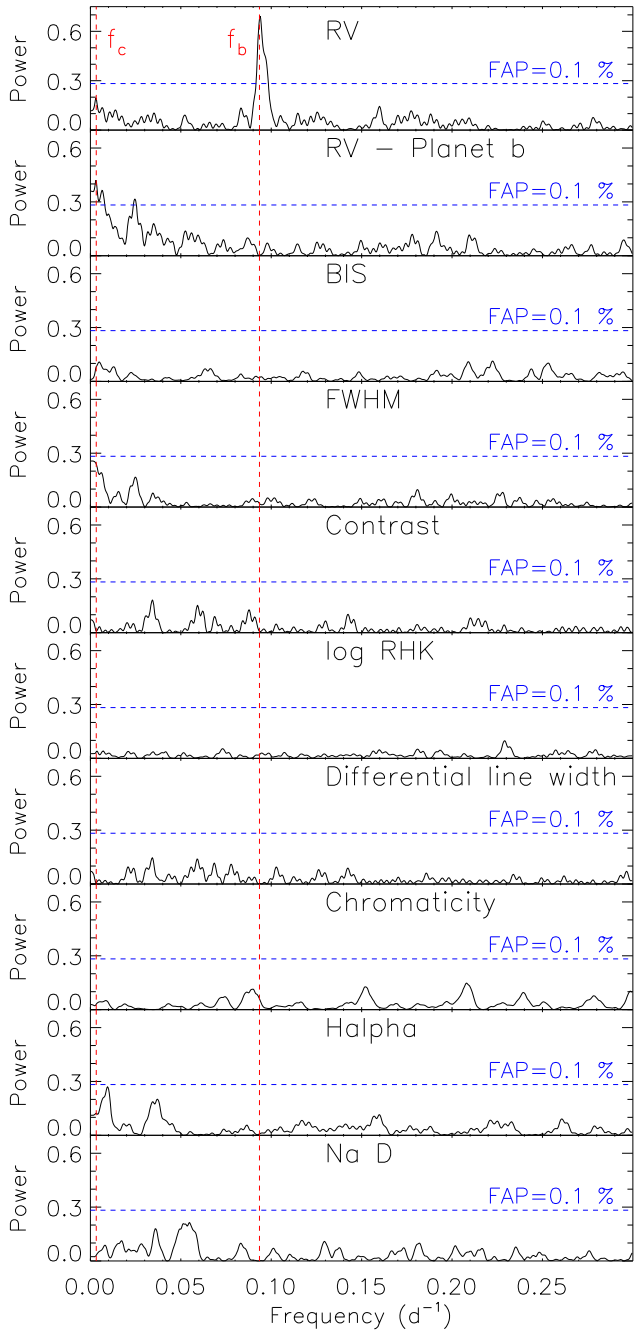

Figure 4. From top to bottom: Generalized Lomb–Scargle periodograms of the HARPS RV measurements (upper panel); the RV residuals following the subtraction of the signal of the transiting planet (second panel); the activity indicators of TOI-220 (remaining panels). The 0.1 per cent false alarm probability (FAP) estimated using the bootstrap method is shown with horizontal dashed lines. The vertical red lines mark the orbital frequencies the transiting planet TOI-220 *b* ($f_b = 0.093\,d^{-1}$) and of the additional Doppler signal we found in the HARPS RVs ($f_c = 0.0032\,d^{-1}$).

that its period is poorly constrained, being comparable to the temporal baseline of our observations (327 d). Moreover, the position of this peak depends on the last poorly sampled measurements. Therefore, as discussed in Section 3.3.2, the exact nature of this long period signal cannot be firmly constrained with the currently available RV data.

3.3 PASTIS analysis

The *Planet Analysis and Small Transit Investigation Software* (Díaz et al. 2014; Santerne et al. 2015), PASTIS, was used for the joint analysis of the transit light curves, the radial velocities, and the spectral energy distribution of TOI-220. The PASTIS package implements a fully Bayesian analysis of the data and uses the Markov Chain Monte Carlo (MCMC) method to sample the posterior distribution of the resulting parameters (see e.g. Santerne et al. 2019; Lopez et al. 2019, and references therein). We draw the posterior distributions of all free parameters after merging the best MCMC chains, i.e. those with the largest model likelihood (log L) from a sample of 30 chains with 10^6 steps each. The convergence of these chains is checked by a Kologorov–Smirnov (K–S) test after the burn-in period (BI) of each chain has been removed. Here, the BI phase corresponds to the initial portion of each chain with a log L mean and variance $2\,\sigma$ away from the corresponding values of the last 10 per cent of the chain. Then, after removing the BI phase, the selected chains correspond to those with a median log L within $2\,\sigma$ of the best chain (i.e. the chain with the largest median log L) and with a K–S test p-value above 10^{-30}.

As mentioned in Section 2, 17 individual transits of TOI-220 *b* were extracted from the *TESS* light curves and input to PASTIS. Additionally, a nightly binning was applied to the RV data in order to minimize the jitter induced by stellar activity and/or granulation, ending up thus with 69 points out of the total 91 RV measurements. The transits were modelled using JKTEBOP software (Southworth 2008) and the RV data using Keplerian orbits.

3.3.1 Stellar SED analysis

PASTIS also models the host star by fitting the spectral energy distribution (SED) to the BT-Settl atmosphere models (Allard, Homeier & Freytag 2012), Dartmouth evolutionary tracks (Dotter et al. 2008) and the quadratic limb darkening coefficients for *TESS* bandpass based on the tables from Claret & Bloemen (2011).

After a preliminary analysis using all the available magnitudes of TOI-220 (Table 1), we obtained a very poor fit of the visual magnitudes, in particular in the V band. We attributed this result to inconsistencies with the magnitude zero-point used or with unreliable V magnitude estimations due to saturation of stars brighter than $V = 10$ mag in the case of the APASS catalogue (Henden et al. 2015). As PASTIS does not implement the use of *Gaia* magnitudes by the time of this analysis, we decided to use only 2MASS (Skrutskie et al. 2006) and AllWISE (Cutri et al. 2014) magnitudes for the bayesian analysis. For this, we took TOI-220's NIR magnitudes as reported in the *TESS* Input Catalogue (TICv8; Stassun et al. 2019). The host star was modelled for the effective temperature, $T_{\rm eff}$; surface gravity, log g; metallicity, [M/H]; distance, d; colour excess, $E(B-V)$; the systemic radial velocity, v_0, using as priors either normal or uniform distributions as presented in Table B1. The SED and best stellar model obtained with PASTIS are displayed in Fig. 5 and the fitted and derived stellar parameters are listed in Table 3. The resulting stellar parameters are consistent within their uncertainties with the values obtained independently from the spectral analysis described in Section 3.1.

In order to corroborate the TOI-220's effective temperature obtained with PASTIS and to discard any bias we could have introduced by using only NIR magnitudes, the observed and theoretical SEDs for TOI-220 were compared using the Virtual Observatory Spectral Analyzer (VOSA; Bayo et al. 2008). The observed SED was constructed using the four IR bands *W1*-*W4* from allWISE, the *J*, *H*, and *Ks* bands from 2MASS (Skrutskie et al. 2006), and also including

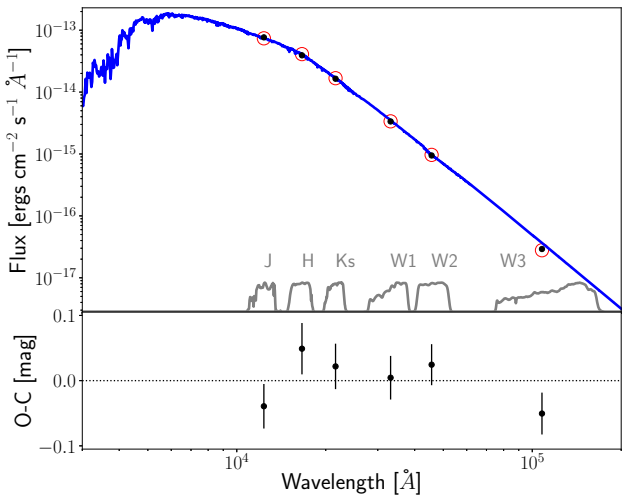

Figure 5. Top panel: spectral energy distribution of TOI-220 with the best stellar atmosphere model from the BT-SETTL library obtained with PASTIS (blue solid line). Residuals are shown in the bottom panel (error bars include the fitted jitter from the analysis).

the three bands from *Gaia* (Gaia Collaboration 2018). As before, the theoretical fluxes were computed from the grids of theoretical stellar spectra BT-Settl (AGSS2009; Allard, Homeier & Freytag 2012). A best fit with the observed data was computed by χ^2 minimization by testing effective temperature values ranging from 1000 to 7000 K with steps of 100 K. We also adopted the estimation of interstellar extinction provided in the *TESS* input catalogue (Stassun et al. 2019), then computing the reddening according to Fitzpatrick (1999) and Schlafly & Finkbeiner (2011). The SED and the fitted stellar model are shown in Fig. A1. This independent analysis provides an effective temperature of 5300 ± 50 K, in very good agreement with the result from PASTIS. This analysis also shows no IR-excess, suggesting the absence of circumstellar material around TOI-220, at least in the *WISE* infrared bands.

3.3.2 *Planetary analysis*

Based on the periodograms presented in Section 3.2, the data analysis of the TOI-220 system was performed taking into account the presence of a single planet in the system to probe the 10.69 d periodic signal. Additionally, we also included a quadratic, long-term RV trend in the modelling.

For the single planet scenario we modelled the planetary orbital period, P; the reference transit epoch, T_0; the star–planet radius ratio, R_s/R_p; the radial velocity semi-amplitude, K; and the inclination, eccentricity, and argument of the periastron of the orbit: i, e, and ω, respectively. The prior distribution used for each parameter is reported in Table B1. The posterior distribution of all the free parameters was drawn from the best 15 MCMC chains after removing the burn-in (BI) time (7–22 per cent of the chain). The full list of fitted and derived parameters of the system together with its respective 68.3 per cent confidence interval are given in Table 3 and 4 for the star and planet, respectively. Despite the good fit of the keplerian model, it seems that a structure is still present in the RV residuals (see e.g. Fig. 4, second panel). To better assess the significance of this trend, we applied the Anderson–Darling (A–D) test (Stephens 1974) to the RV residuals (Table D1). The A–D test is a modification of the K–S test to evaluate whether a data sample comes from a specific distribution; in our case we tested the RV residuals against a normal distribution. The test's result is compared then to a set of critical values in a range of significance levels. In particular, the A–D test statistic (see Table D1) of the RV residuals is greater than the critical value at 15 per cent significance, $0.580 > 0.547$ ($\alpha = 0.15$), therefore the normality hypothesis of the RV residuals is rejected evidencing that they may contain astrophysical information not included in our single planet model.

Therefore, we also explored the effect of including a radial velocity quadratic trend in the RV modelling. For this, we used the same initial setup as before but adding two extra terms to account for a quadratic drift in the stellar radial velocity. We set a wide uniform distribution as a prior for the amplitude of the drift coefficients (Table B1). Here, we selected the best 20 MCMC chains after removing the BI (7–27 per cent of the chain) to draw the posterior distributions of the fitted parameters. The fitted drift coefficients are reported in Table 3

Table 3. Stellar properties of TOI-220.

Parameter	Value	Ref.
$T_{\rm eff}$ (K)	5273 ± 115	(1)
$T_{\rm eff}$ (K) (adopted)	5298 ± 65	(2)
$T_{\rm eff}$ (K)	5384 ± 77	(3)
$T_{\rm eff}$ (K)	5182 ± 45	(4)
log g (cgs) (adopted)	4.37 ± 0.11	(2)
log g (cgs)	4.25 ± 0.07	(4)
log g (cgs)	4.49 ± 0.03	(3)
$V_{\rm turb}$ (km s^{-1})	0.694 ± 0.058	(2)
[Fe/H] (dex)	-0.217 ± 0.044	(2)
[M/H] (dex)	-0.19 ± 0.05	(3)
[Fe/H] (dex)	-0.2 ± 0.07	(4)
[Mg/H] (dex)	-0.10 ± 0.05	(2)
[Si/H] (dex)	-0.14 ± 0.04	(2)
[O/H] (dex)	-0.031 ± 0.072	(2)
[C/H] (dex)	-0.214 ± 0.045	(2)
[Cu/H] (dex)	-0.176 ± 0.044	(2)
[Zn/H] (dex)	-0.172 ± 0.027	(2)
[Sr/H] (dex)	-0.156 ± 0.077	(2)
[Y/H] (dex)	-0.293 ± 0.094	(2)
[Zr/H] (dex)	-0.236 ± 0.071	(2)
[Ba/H] (dex)	-0.237 ± 0.025	(2)
[Ce/H] (dex)	-0.166 ± 0.045	(2)
[Nd/H] (dex)	-0.100 ± 0.039	(2)
$v \sin i$ (km s^{-1})	2.90 ± 0.35	(4)
$V_{\rm mac}$ (km s^{-1})	0.9 ± 0.4	(4)
$V_{\rm mic}$ (km s^{-1})	0.85 ± 0.10	(4)
Age (Gyr) (adopted)	10.1 ± 1.4	(2)
Age (Gyr)	$10.7^{+2.1}_{-3.1}$	(3)
Distance (pc)	89 ± 4	(3)
$E(B-V)$ (mag)	0.163 ± 0.087	(3)
Systemic RV, v_0 (km s^{-1})	26.45827 ± 0.00037	(3)
RV drift lin. coeff. (m s^{-1} d^{-1})	$-0.0379(80)$	(3)
RV drift quad. coeff. (m s^{-1} d^{-2})	0.000149(31)	(3)
Radius [$R_\odot$]	0.858 ± 0.032	(3)
Mass [$M_\odot$]	0.825 ± 0.028	(3)
Density [$\rho_\odot$]	1.31 ± 0.15	(3)
Limb darkening coeff. $u_a^{\rm TESS}$	0.352 ± 0.014	(3)
Limb darkening coeff. $u_b^{\rm TESS}$	0.2475 ± 0.0077	(3)

Notes. (1) TIC v8 (Stassun et al. 2019).
(2) From spectral analysis (Section 3.1). Values correspond to weighted average and the standard deviation.
(3) From PASTIS analysis (Section 3.3). Derived values assume $R_\odot = 695\,508$ km and $M_\odot = 1.98842 \times 10^{30}$ kg.
(4) From spectral analysis validation (Appendix A).

Table 4. Results on the planetary parameters obtained from PASTIS simultaneous analysis of the data assuming a single planet system and by including a long-term quadratic drift in the RVs. Derived values assume $M_\oplus = 5.9736 \times 10^{24}$ kg, $R_\oplus = 6\,378\,137$ m, AU = 149 597 870.7 km, and zero albedo for the equilibrium temperature.

Parameter (fitted)	1 Planet	1 Planet + RV drift (adopted)
Orbital period, P (d)	10.695264(87)	10.695264(86)
Reference transit time, T_0 [BJD−TDB]	2458335.9021(14)	2458335.9020(14)
Planet-to-star radius ratio, R_p/R_s	0.03227 ± 0.00078	0.03235 ± 0.00076
Orbital inclination, i (°)	87.86 ± 0.14	87.88 ± 0.12
RV semi-amplitude, K ($m\,s^{-1}$)	4.47 ± 0.36	4.56 ± 0.32
Orbital eccentricity, e	$0.029^{+0.034}_{-0.021}$	$0.032^{+0.038}_{-0.023}$
Argument of periastron, ω (°)	159 ± 150	248^{+66}_{-190}
Parameter (derived)		
Mass [$M_\oplus$]	13.6 ± 1.2	13.8 ± 1.0
Radius [$R_\oplus$]	3.02 ± 0.17	3.03 ± 0.15
bulk density, ρ_p ($g\,cm^{-3}$)	2.69 ± 0.55	2.73 ± 0.47
System scale, a/R_s	22.3 ± 1.0	22.33 ± 0.80
Impact parameter, b	0.832 ± 0.026	0.836 ± 0.022
Transit duration, T_{14} (h)	2.231 ± 0.054	2.239 ± 0.055
orbital semi-major axis, a (AU)	0.08920 ± 0.0010	0.08911 ± 0.0010
Mean equilibrium temperature, T_{eq} (K)	806 ± 25	805 ± 21
Instrument-related parameters		
HARPS jitter ($m\,s^{-1}$)	1.71000 ± 0.00021	1.35000 ± 0.00024
SED jitter (mag)	0.048 ± 0.025	0.049 ± 0.026
TESS jitter (ppm)	111 ± 74	111 ± 74
TESS out-of-transit flux	1.000093(30)	1.000093(30)

and the RV drift together with the 1-planet model are shown in Fig. 7. Despite the amplitude of the residuals being smaller when compared to the single planet scenario, the structure in the first epochs ($t <$ 2458440.20 BJD) in the RV residuals seems to remain. But in this case, the normality of the residuals is not rejected by the A–D test. We show in Table D1 the result of this and other statistical tests which favour the inclusion of the RV drift in the modelling. Notably, the TOI-220 *b* parameters are not affected by including this RV long-term drift (Table 4). In Appendix E we show the mass constraints of a hypothetical second orbital body based on the estimated RV drift. Finally, we also checked the results when including a second planet in the modelling with a wide prior in the orbital period around the peak observed in the RV residual periodogram (300 ± 100 d). We found that the RMS of the RV residuals are reduced, however, the resulting parameters for the second planet are poorly constrained. Based on this together with the fact that all the obtained parameters of TOI-220 *b* remain fully compatible between models (see Table 4); and specially considering the baseline of the RV monitoring (only 327 d compared with the periodogram peak of the RV residuals of ∼309 d) and that the location of this peak strongly depends on the data points considered to calculate the periodogram; we adopt the values derived using the 1-planet with the quadratic RV long-term drift shown in Tables 3 and 4 for the star and planet, respectively. We obtained for TOI-220 *b* a planetary mass and radius of $M_p = 13.8 \pm 1.0\,M_\oplus$ and R_p=3.03 ± 0.15 $R_\oplus$. The fitted orbital period and reference epoch are $P = 10.695264(86)$ d and $T_0 = 2458335.9020(14)$ [BJD_TDB], respectively. The best model for each individual transit is shown in Fig. 1 and in Fig. 6 for the complete folded light curve of the 17 *TESS* transits. The best RV model including the RV quadratic drift and its residuals are displayed in Fig. 7. As a sanity check, we performed an independent joint analysis of the transit photometry and HARPS Doppler measurements using the code `pyaneti` (Barragán, Gandolfi & Antoniciello 2019). We adopted the same PASTIS RV models and found consistent results well within the nominal error bars, corroborating the results of our analysis.

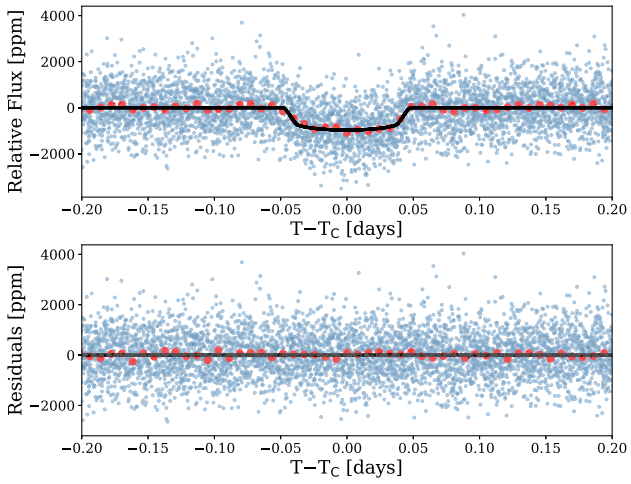

Figure 6. Top: TOI-220 *b* transit light curve built by joining the 17 *TESS* transits used in this work (blue points and 12 min bins in red) together with the best model (solid curve) obtained with PASTIS analysis. The residuals are shown in the bottom panel.

3.4 Transit timing variations

We performed the timing analysis of TOI-220 *b* using the 17 *TESS* transits from sectors 1–12, the 4 transits of sectors 27–28; and the 2 transit observations obtained with the LCOGT telescopes. For this, we fixed all the transit parameters to the values obtained from PASTIS analysis in Section 3.3.2 except for the T_c, R_p/R_s and the inclination which were let free to vary. As the two LCOGT transits have a relative lower quality in terms of photometric precision and sampling; and owing to the fact that they cover only the ingress of the transit (see Fig. F1) we fixed also the inclination to $i = 87.88$ deg for the modelling of these light curves. For the mid-times of the

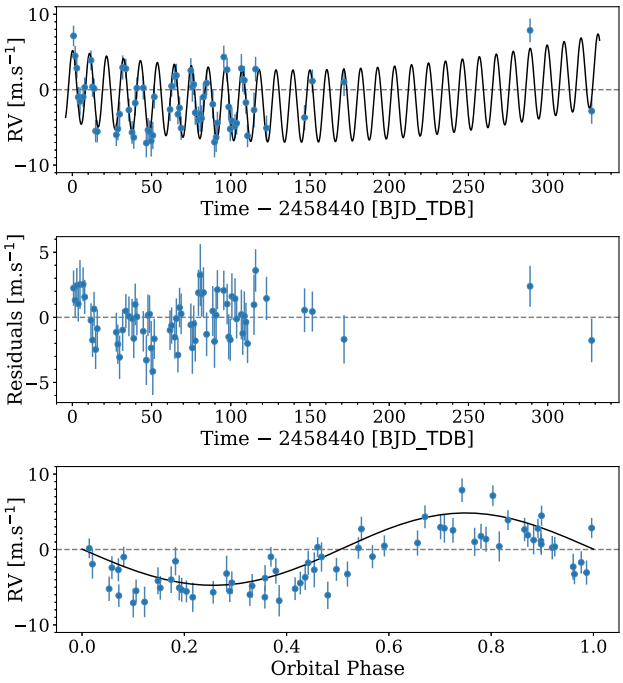

Figure 7. Radial velocity time-series with the best fitted model superimposed with the corresponding residuals are shown in the top and middle panel, respectively. The phased radial velocity measurements are shown in the bottom panel. The error bars include the fitted jitter for each case. Additional, a fitted quadratic long-term is represented by a solid red curve in the middle panel (see Section 3.3.2 for details).

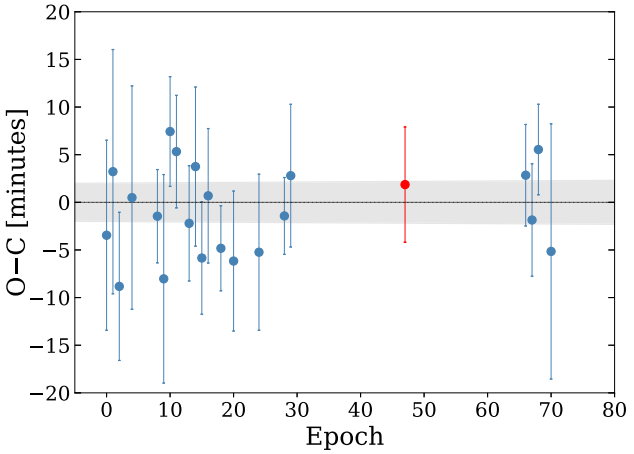

Figure 8. Observed minus calculated diagram of the transit mid-times of TOI-220 *b*. The blue symbols correspond to *TESS* transits while the red symbol correspond to the second LCOGT transit observation. The shaded region represents the projected 1σ uncertainties of ephemeris equation of TOI-220 *b* (Section 3.4).

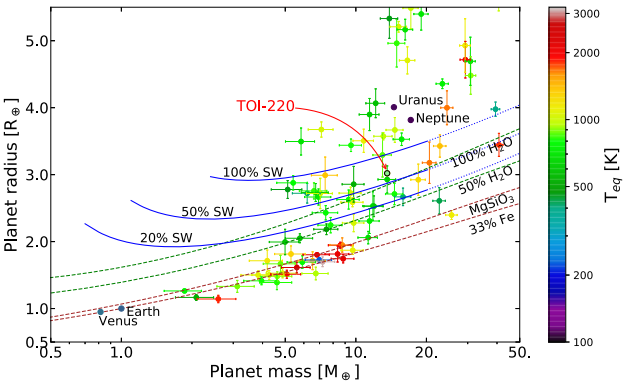

Figure 9. Mass–radius diagram of the confirmed exoplanets with mass and radius measurements better than 20 per cent and 10 per cent, respectively. The symbol's colour scales with the equilibrium temperature of the planet. TOI-220 *b* location in the diagram is highlighted with the red arrow and black circle. Solar System planets are also shown for reference. Composition models from Zeng et al. (2019) are displayed with dash brown and green lines. Those for a planet at 800 K with an Earth-like composition topped with various proportion of a steam and supercritical water layer (Mousis et al. 2020) are displayed with blue solid lines.

TESS transits, we used as priors a normal distribution with a 0.4 d width centred in the values obtained from the BLS analysis (Table 2). For each transit fit we used 20 MCMC chains of 10^5 iterations. The obtained values for R_p/R_s and inclination are consistent within the uncertainties in all the transits. The resulting transit mid-times are reported in Table F1. The average uncertainty of the transit mid-times is around 7 min. The first LCOGT transit has an uncertainty larger than 30 min in comparison with the 6 min of second LCOGT transit. As this light curve has a very poor photometric quality and transit coverage, we removed it from the analysis. With the obtained mid-times and the ephemeris equation:

$$T_c(n) = 2458335.9021(14)[\mathrm{BJD\_TBD}] + n \times 10.695264(86), \quad (1)$$

where P and T_0 are from Section 3.3.2; we estimated the timing residuals of TOI-220 *b* as presented in Fig. 8 and Table F1. All the transit times are consistent within the uncertainties with a constant orbital period; the RMS of the O−C points is around 4.7 min. In addition, the statistical A–D test supports the hypothesis that the timing residuals are drawn from a normal distribution, discarding thus, orbital perturbations induced by a possible close companion.

4 PLANETARY STRUCTURE

Fig. 9 shows the mass–radius diagram of all the confirmed exoplanets to date,[8] with a precision better than 20 per cent and 10 per cent in their mass and radius, respectively. TOI-220 *b* is well located in a domain of the sub-Neptune size planets. We investigate the interior of TOI-220 *b* in order to get some insights into its composition. To that purpose, we used the model of internal structure developed by Brugger et al. (2017) and recently updated by Mousis et al. (2020) to include a steam and supercritical water layer for the special case of highly irradiated planets. When the pressure and temperature are above the critical point of water, water is in supercritical phase. To describe this water layer, we use the Equation of State (EOS) of Mazevet et al. (2019), which includes experimental and theoretical data of water at pressures and temperatures higher than the critical point of water. TOI-220 *b* being strongly irradiated with an equilibrium temperature of 806 K, the model allows us to address how its composition could differ from that of a Neptune-like planet with a large gaseous envelope overlying a rocky core. We followed the method described in Lillo-Box et al. (2020) and Acuña et al. (2021) exploring the core mass fraction (CMF, the ratio of the mass of the core and the total planetary mass) and the water mass fraction (WMF,

[8] from http://exoplanet.eu/ as of 2021 January 27.

Table 5. Output parameters retrieved by the MCMC interior and atmosphere modelling.

Parameter	Value
Total mass, M_p [$M_\oplus$]	13.8 ± 0.7
Total radius, R_p [$R_\oplus$]	3.06 ± 0.12
Total density, ρ_p (g cm^{-3})	2.65 ± 0.28
Core mass fraction, CMF	0.08 ± 0.03
Water mass fraction, WMF	0.62 ± 0.10
Fe/Si mole ratio	0.64 ± 0.11
Mg/Si mole ratio	1.16 ± 0.10
Mg number, # Mg	0.85–1.0
Temperature at 300 bar, T_{surf} (K)	3536 ± 203
Planetary albedo, a_p	0.230 ± 0.001
Atmospheric thickness, z (km)	1111 ± 99
Atmospheric mass, M_{atm} ($M_\oplus$ 10^{-3})	1.31 ± 0.16
Core+Mantle radius, (R_p units)	0.47 ± 0.05

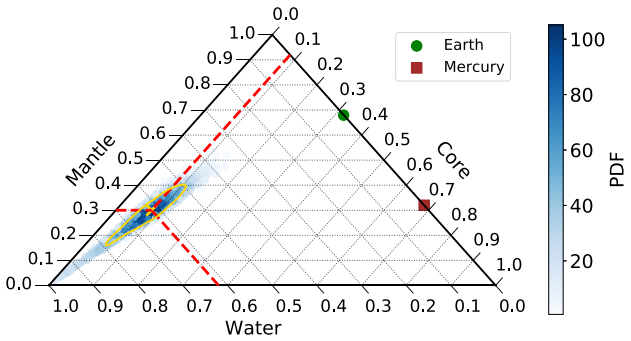

Figure 10. Sampled 2D marginal posterior distribution function for the CMF and WMF of TOI-220 *b* (blue region). The PDF mean and the 1σ confidence interval is marked by the yellow cross and curve, respectively. TOI-220 *b* is consistent with a water-rich planet (WMF = 0.62 ± 0.10) with a very small core (CMF = 0.08 ± 0.03). Earth and Mercury values are presented for comparison.

the ratio of the mass of the water layer – steam and supercritical – and the total mass) of the planet as free parameters in an MCMC Bayesian framework adapted from Dorn et al. (2015).

We use as input parameters the planetary mass and radius, and the Fe/Si and Mg/Si mole ratios. The latter are calculated with the stellar abundances in Table 3 as Fe/Si = 0.65 ± 0.09 and Mg/Si = 1.17 ± 0.17. The code allows us to explore the posterior distribution functions of three compositional parameters: CMF, WMF, and the Mg number (# Mg), which is a proxy for the level of differentiation of the planet as described by Sotin, Grasset & Mocquet (2007) and Brugger et al. (2017). If most of the Mg is located in the mantle and Fe in the core, the planet is highly differentiated and # Mg is close to one (0.9 for the case of Earth). On the contrary, if Mg and Fe are mixed in the mantle, # Mg will have lower values (≃0.6). In the MCMC algorithm, we assume uniform prior distributions of the CMF, WMF, and the Mg number.

Table 5 shows the retrieved values of the three free compositional parameters, in addition to the observables (mass, radius, and mole ratios), and the atmospheric variables. The posterior distributions of the CMF and WMF are also shown in Fig. 10. We used an MCMC algorithm to obtain samples of the posterior distribution of all our observable parameters: mass, radius, Fe/Si, and Mg/Si. Convergence is achieved when the output parameters of the model reproduce the observed values within the 1σ confidence intervals. Our results indicate that a planetary structure composed of a core rich in Fe,

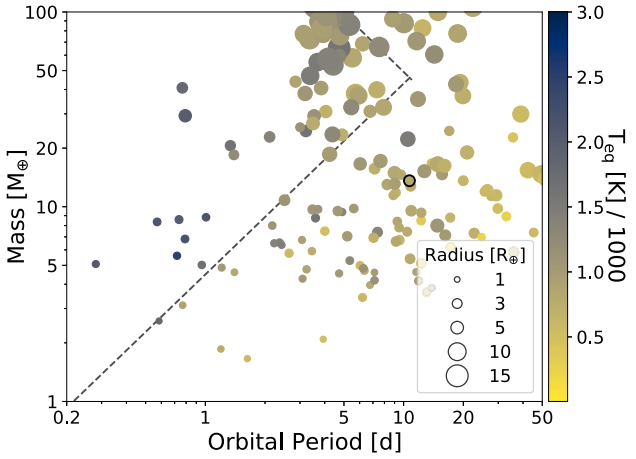

Figure 11. Mass–period diagram of the confirmed exoplanets to date with masses and periods below 100 $M_\oplus$ and 50 d, respectively (same planets sample as Fig. 9). The symbols size represents the radius of the planet while its equilibrium temperature is coded by the colour of the symbol. TOI-220 *b* is outlined with a black circle. The dashed lines mark the edges of the Neptune-desert from Mazeh, Holczer & Faigler (2016).

a silicate mantle, and a supercritical water layer topped by a steam atmosphere in radiative–convective equilibrium is a likely scenario for TOI-220 *b*.

Since its host star is less enriched in Fe than the Sun and Earth (Fe/Si = 0.93), its CMF is significantly lower (0.08 ± 0.03) than the terrestrial value, 0.32. As can be seen in Table 5, the large # Mg obtained (0.85–1.0) is indicative of a highly differentiated core and mantle configuration such as the Earth (# Mg = 0.9). Furthermore, as shown in Fig. 10, TOI-220 *b* could be a water-rich planet with a minimum WMF of 52 per cent, which is compatible with the composition derived for water-rich satellites in the Solar System, such as Titan, and a maximum WMF of 72 per cent, which is below the average water proportion found in comets (see fig. 12 of McKay et al. 2019). Moreover, most of the water mass would be under pressure and temperature conditions beyond the supercritical point, forming a supercritical and steam water layer that would constitute 47 per cent of the total radius.

5 DISCUSSION

The combined analysis of the photometric and spectroscopic data has fully confirmed the planetary nature of the TOI-220 *b* transiting candidate. We noted the presence of a structure in the RV residuals on the exact nature of which, instrumental or planetary, we could not conclude with the data currently available. Therefore, any further investigation of the long-period signals would require additional RVs. Thus, we adopt the values derived using a single planet model in the system and including a quadratic long-term trend in the RVs. In Fig. 11 we show the mass–period diagram of all the confirmed exoplanets including TOI-220 *b* (same sample as Fig. 9). The symbol size scales with the radii of planets while the colour represents the planet's equilibrium temperature. TOI-220 *b* is located in the region of the warm sub-Neptunes class of exoplanets (T_{eq} < 1000 K) with a relatively large size (3 $R_\oplus$).

A paucity of exoplanets has been reported in the planet size distribution around 1.5–2.0 $R_\oplus$ (e.g. Fulton et al. 2017; Fulton & Petigura 2018; Van Eylen et al. 2018), in particular for a $M_\star \sim$ 0.8 $M_\odot$ the gap is around 1.6 $R_\oplus$. It is suggested that this gap is

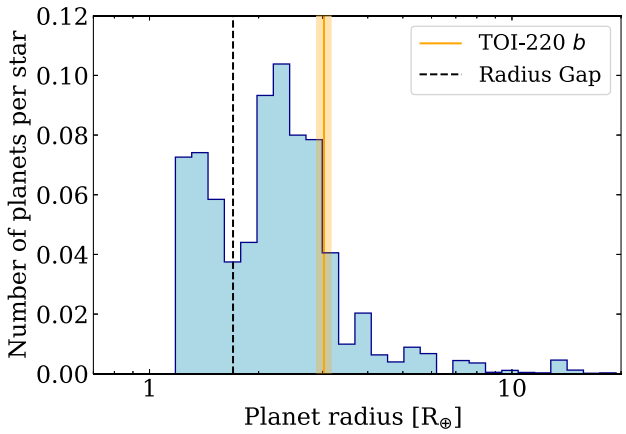

Figure 12. Histogram of the planetary radius for planets with periods below 100 d as presented in Fulton & Petigura (2018). The location of the radius gap and the size of TOI-220 *b* ($\pm 1\,\sigma$) are shown with the black-dashed and orange-shaded lines, respectively.

driven by photoevapouration mass-loss which acts shifting planets with gaseous envelopes towards a rocky Super-Earth population ($R < 1.7\,R_\oplus$). TOI-220 *b* lies above the gap in the Fulton's diagram (see Fig. 12) in the not so populated high end of the size distribution of planets ($R \gtrsim 3\,R_\oplus$) orbiting low mass stars ($M_\star < 0.97\,M_\odot$), as can be seen in figs 8 and 9 in Fulton & Petigura (2018). The atmospheric composition of TOI-220 *b*, either with a thick H/He layer or water-rich content, suggests a formation in the protoplanetary disc past the snow line followed by slow migration. The host's age of ∼10 Gyr points to a very evolved system and the large planet's radius suggests the planet was massive enough to keep its atmosphere despite the large irradiation received by its host star. To get a first estimate of the atmospheric escape of TOI-220 *b*, we used equations of Aguichine et al. (2021). We found that the mass lost by Jeans' escape is negligible even for light species (H/He) due to the surface gravity of the planet. Only $\sim 0.1\,M_\oplus$ could be removed by XUV photoevapouration along its 10.1 Gyr of life. This picture is consistent with the idea that the fate of warm sub-Neptunes located above the gap in the Fulton's diagram (Fig. 12) is not to end their evolution as naked cores (see Deleuil et al. 2020; Bean, Raymond & Owen 2021, and references therein). Precise measurements of physical parameters of planets and its host stars, like the ones presented in this work, are key to shape the knowledge of the formation and evolution processes that sculpt the planet population in this region of parameter space.

Complementarily, we have performed an interior structure and atmosphere analysis within a Bayesian framework to constrain the composition of TOI-220 *b* given its density and the stellar abundances of the host star. The low density of this strongly irradiated planet could be explained with a water-rich atmosphere that reaches the supercritical phase at its base, with a silicate mantle and an iron core as its bulk. As an alternative the planet might have a solid core surrounded by a thick H/He atmosphere. Future work should explore this possibility but also a composition with a well-mixed water and H/He atmosphere, since these are the most common volatiles that can form low-mass planets. The confirmation of the water-rich atmosphere scenario would also require conducting atmospheric characterization to search for water spectral features. Following Kempton et al. (2018), we thus calculate TOI-220 *b* transmission spectroscopy metric to check whether the planet would be amenable to such a characterization by *JWST* or the ELT. We obtained a value of 45, which is well below the threshold of 84 for planets in this range of size, making of TOI-220 *b* atmosphere likely out of reach for the next decade.

ACKNOWLEDGEMENTS

SH acknowledges the Centre National d'Etudes Spatiales (CNES) funding through the grant 837319. MD acknowledges the CNES support. VA, EDM, SGS, NCS, SCCB, and SHoj acknowledge support by FCT – Fundação para a Ciência e a Tecnologia (Portugal) through national funds and by FEDER through COMPETE2020 – Programa Operacional Competitividade e Internacionalização by these grants: UID/FIS/04434/2019; UIDB/04434/2020; UIDP/04434/2020; PTDC/FIS-AST/32113/2017 & POCI-01-0145-FEDER-032113; PTDC/FIS-AST/28953/2017 & POCI-01-0145-FEDER-028953. VA, EDM, SCCB, SGS, and ODSD further acknowledge the support from FCT through Investigador FCT contracts IF/00650/2015/CP1273/CT0001, IF/00849/2015/CP1273/CT0003, IF/01312/2014/CP1215/CT0004, CEECIND/00826/2018–POPH/FSE(EC), and DL57/2016/CP1364/CT0004, respectively. SHoj further acknowledges the support by FCT through the fellowship PD/BD/128119/2016. DJA acknowledges support from the STFC via an Ernest Rutherford Fellowship (ST/R00384X/1). LMS and DG gratefully acknowledge financial support from the CRT foundation under Grant No. 2018.2323 'Gaseous or rocky? Unveiling the nature of small worlds'. JRM, BLCM, and ICL acknowledge continuous grants from the brazilian funding agencies CNPq, CAPES, and FAPERN. This study was financed in part by the Coordenação de Aperfeiçoamento de Pessoal de Nível Superior-Brasil (CAPES)-Finance Code 001. PK and JS acknowledge the MSMT INTER-TRANSFER grant LTT20015. This paper includes data collected with the *TESS* mission, which are publicly available from the Mikulski Archive for Space Telescopes (MAST). Funding for the *TESS* mission is provided by NASA's Science Mission directorate. We acknowledge the use of public *TESS* Alert data from pipelines at the *TESS* Science Office and at the *TESS* Science Processing Operations Center. This research has made use of the Exoplanet Follow-up Observation Program website, which is operated by the California Institute of Technology, under contract with the National Aeronautics and Space Administration under the Exoplanet Exploration Program. Resources supporting this work were provided by the NASA High-End Computing (HEC) Program through the NASA Advanced Supercomputing (NAS) Division at Ames Research Center for the production of the SPOC data products. This research has made use of computing facilities operated by CeSAM data center at LAM, Marseille, France; and the Data & Analysis Center for Exoplanets (DACE), which is a facility based at the University of Geneva (CH) dedicated to extrasolar planets data visualization, exchange, and analysis. DACE is a platform of the Swiss National Centre of Competence in Research (NCCR) PlanetS, federating the Swiss expertise in Exoplanet research. This research has made use of data obtained from the portal exoplanet.eu of The Extrasolar Planets Encyclopaedia. This research has made use of the NASA Exoplanet Archive, which is operated by the California Institute of Technology, under contract with the National Aeronautics and Space Administration under the Exoplanet Exploration Program. This work makes use of observations from the LCOGT network. DG warmly thanks Alessia Barbiero and Pietro Giordano for the inspiring conversations at the time the HARPS follow-up of TOI-220 was started in 2018 November.

Software: We gratefully acknowledge the open source software which made this work possible: `astropy` (Astropy Collaboration 2013; Price-Whelan et al. 2018), `ipython` (Pérez & Granger 2007), `numpy` (Van Der Walt, Colbert & Varoquaux 2011), `scipy` (Jones et al. 2001), `matplotlib` (Hunter 2007), `jupyter` (Kluyver et al. 2016), `pandas` (McKinney 2010; Pandas development team. 2020).

Facilities: *TESS*, ESO: 3.6 m (HARPS spectrograph), Gemini: South (Zorro), LCOGT, Exoplanet Archive

This work is based on observations made with ESO Telescopes at the La Silla Observatory under programs ID 1102.C-0923, 1102.C-0249, 0102.C-0584, 60.A.9700, and 60.A-9709.

DATA AVAILABILITY

The TESS photometric data used in this work is available via Mikulski Archive for Space Telescopes (MAST) archive and TFOP program. Radial velocity measurements and the derived stellar activity indicators are provided in Tables G1 and G2, respectively. These tables are also available in digital form in the online version of the manuscript.

REFERENCES

Acuña L., Deleuil M., Mousis O., Marcq E., Levesque M., Aguichine A., 2021, A&A, 647, A53

Adibekyan V. et al., 2015, A&A, 583, A94

Adibekyan V. Z., Sousa S. G., Santos N. C., Delgado Mena E., González Hernández J. I., Israelian G., Mayor M., Khachatryan G., 2012, A&A, 545, A32

Aguichine A., Mousis O., Deleuil M., Marcq E., 2021, preprint (arXiv:2105.01102)

Akeson R. L. et al., 2013, PASP, 125, 989

Allard F., Homeier D., Freytag B., 2012, Phil. Trans. R. Soc. A, 370, 2765

Aller A., Lillo-Box J., Jones D., Miranda L. F., Barceló Forteza S., 2020, A&A, 635, A128

Armstrong D. J. et al., 2020, Nature, 583, 39

Astropy Collaboration, 2013, A&A, 558, A33

Barragán O., Gandolfi D., Antoniciello G., 2019, MNRAS, 482, 1017

Bayo A., Rodrigo C., Barrado Y Navascués D., Solano E., Gutiérrez R., Morales-Calderón M., Allard F., 2008, A&A, 492, 277

Bean J. L., Raymond S. N., Owen J. E., 2021, J. Geophys. Res., 126, e06639

Bensby T., Feltzing S., Lundström I., 2003, A&A, 410, 527

Bertran de Lis S., Delgado Mena E., Adibekyan V. Z., Santos N. C., Sousa S. G., 2015, A&A, 576, A89

Bhatti W., Bouma L. G., Wallace J., 2020, Zenodo, Astrobase

Brown T. M. et al., 2013, PASP, 125, 1031

Brugger B., Mousis O., Deleuil M., Deschamps F., 2017, ApJ, 850, 93

Bruntt H. et al., 2010, A&A, 519, A51

Canto Martins B. L. et al., 2020, ApJS, 250, 20C

Carleo I. et al., 2020, AJ, 160, 114C

Chabrier G., 2001, ApJ, 554, 1274

Claret A., Bloemen S., 2011, A&A, 529, A75

Collier Cameron A. et al., 2019, MNRAS, 487, 1082

Collins K. A., Kielkopf J. F., Stassun K. G., Hessman F. V., 2017, AJ, 153, 77

Crossfield I. J. M., Kreidberg L., 2017, AJ, 154, 261

Cutri R. M. et al., 2014, VizieR Online Data Catalog: AllWISE Data Release

Deleuil M., Pollacco D., Baruteau C., Rauer H., Blanc M., 2020, Space Sci. Rev., 216, 105

Delgado Mena E., Israelian G., González Hernández J. I., Bond J. C., Santos N. C., Udry S., Mayor M., 2010, ApJ, 725, 2349

Delgado Mena E., Tsantaki M., Adibekyan V. Z., Sousa S. G., Santos N. C., González Hernández J. I., Israelian G., 2017, A&A, 606, A94

Delgado Mena E. et al., 2014, A&A, 562, A92

Delgado Mena E. et al., 2019, A&A, 624, A78

Díaz R. F., Almenara J. M., Santerne A., Moutou C., Lethuillier A., Deleuil M., 2014, MNRAS, 441, 983

Dorn C., Khan A., Heng K., Connolly J. A. D., Alibert Y., Benz W., Tackley P., 2015, A&A, 577, A83

Dotter A., Chaboyer B., Jevremović D., Kostov V., Baron E., Ferguson J. W., 2008, ApJS, 178, 89

Doyle A. P., Davies G. R., Smalley B., Chaplin W. J., Elsworth Y., 2014, MNRAS, 444, 3592

Dumusque X. et al., 2015, ApJ, 814, L21

Fitzpatrick E. L., 1999, PASP, 111, 63

Fridlund M. et al., 2020, MNRAS, 498, 4503

Fulton B. J., Petigura E. A., 2018, AJ, 156, 264

Fulton B. J. et al., 2017, AJ, 154, 109

Gaia Collaboration, 2018, A&A, 616, A1

Gandolfi D. et al., 2018, A&A, 619, L10

Gao P. et al., 2020, Nat. Astron., 4, 951

Ginzburg S., Schlichting H. E., Sari R., 2018, MNRAS, 476, 759

Girardi L. et al., 2012, Astrophys. Space Sci. Proc., 26, 165

Guerrero N. M. et al., 2021, preprint (arXiv:2103.12538)

Gupta A., Schlichting H. E., 2019, MNRAS, 487, 24

Hall J. C., Lockwood G. W., Skiff B. A., 2007, AJ, 133, 862

Henden A. A., Levine S., Terrell D., Welch D. L., 2015, American Astronomical Society Meeting Abstracts #225, 336.16

Howell S. B., Everett M. E., Sherry W., Horch E., Ciardi D. R., 2011, AJ, 142, 19

Hunter J. D., 2007, Comput. Sci. Eng., 9, 90

Jenkins J. M., 2002, ApJ, 575, 493

Jenkins J. M. et al., 2010, in Radziwill N. M., Bridger A., eds, Proc. SPIE Conf. Ser. Vol. 7740, Software and Cyberinfrastructure for Astronomy. SPIE, Bellingham, p. 77400D

Jenkins J. M. et al., 2016, in Chiozzi G., Guzman J. C., Proc. SPIE Conf. Ser. Vol. 9913, Software and Cyberinfrastructure for Astronomy IV. SPIE, Bellingham, p. 99133E

Jenkins J. S. et al., 2020, Nat. Astron., 4, 1148

Jensen E., 2013, Tapir: A web interface for transit/eclipse observability, ascl, ascl:1306.007

Johnson D. R. H., Soderblom D. R., 1987, AJ, 93, 864

Jones E. et al., 2001, SciPy: Open source scientific tools for Python. Available at: http://www.scipy.org/

Kempton E. M.-R. et al., 2018, PASP, 130, 114401

Kluyver T. et al., 2016, in Loizides F., Schmidt B., eds, Positioning and Power in Academic Publishing: Players, Agents and Agendas. IOS Press, Amsterdam, p. 87

Kurucz R. L., 1993, SYNTHE spectrum synthesis programs and line data

Li J., Tenenbaum P., Twicken J. D., Burke C. J., Jenkins J. M., Quintana E. V., Rowe J. F., Seader S. E., 2019, PASP, 131, 024506

Lillo-Box J., Barrado D., Bouy H., 2014, A&A, 566, A103

Lillo-Box J. et al., 2020, A&A, 640, A48

Lopez T. A. et al., 2019, A&A, 631, A90

Lovis C., Pepe F., 2007, A&A, 468, 1115

Mayor M. et al., 2003, Messenger, 114, 20

Mazeh T., Holczer T., Faigler S., 2016, A&A, 589, A75

Mazevet S., Licari A., Chabrier G., Potekhin A. Y., 2019, A&A, 621, A128

McKay A. J. et al., 2019, AJ, 158, 128

McKinney W., 2010, Proceedings of the 9th Python in Science Conference, 445, 56

Morley C. V., Fortney J. J., Marley M. S., Zahnle K., Line M., Kempton E., Lewis N., Cahoy K., 2015, ApJ, 815, 110

Mousis O., Deleuil M., Aguichine A., Marcq E., Naar J., Aguirre L. A., Brugger B., Gonçalves T., 2020, ApJ, 896, L22

Murdoch K. A., Hearnshaw J. B., Clark M., 1993, ApJ, 413, 349

Nielsen L. D. et al., 2020, MNRAS, 492, 5399

Owen J. E., Lai D., 2018, MNRAS, 479, 5012

Pandas development team, 2020, pandas-dev/pandas: Pandas

Pérez F., Granger B. E., 2007, Comput. Sci. Eng., 9, 21

Pepe F. et al., 2002, Messenger, 110, 9
Piskunov N., Valenti J. A., 2017, A&A, 597, A16
Price-Whelan A. M. et al., 2018, AJ, 156, 123
Ricker G. R. et al., 2015, J. Astron. Telesc. Instrum. Syst., 1, 014003
Santerne A., et al., 2019, preprint (arXiv:1911.07355)
Santerne A. et al., 2015, MNRAS, 451, 2337
Santos N. C. et al., 2013, A&A, 556, A150
Schlafly E. F., Finkbeiner D. P., 2011, ApJ, 737, 103
Schönrich R., Binney J., Dehnen W., 2010, MNRAS, 403, 1829
Skrutskie M. F. et al., 2006, AJ, 131, 1163
Smith J. C. et al., 2012, PASP, 124, 1000
Sneden C. A., 1973, PhD thesis. The University of Texas, Austin
Sotin C., Grasset O., Mocquet A., 2007, Icarus, 191, 337
Sousa S. G., 2014, Determination of Atmospheric Parameters of B-, A-, F- and G-Type Stars, p. 297
Sousa S. G., Santos N. C., Adibekyan V., Delgado-Mena E., Israelian G., 2015, A&A, 577, A67
Southworth J., 2008, MNRAS, 386, 1644
Stassun K. G. et al., 2019, AJ, 158, 138
Stephens M. A., 1974, J. Am. Stat. Assoc., 69, 730
Stumpe M. C., Smith J. C., Catanzarite J. H., Van Cleve J. E., Jenkins J. M., Twicken J. D., Girouard F. R., 2014, PASP, 126, 100
Stumpe M. C. et al., 2012, PASP, 124, 985
Szabó G. M., Kiss L. L., 2011, ApJ, 727, L44
Twicken J. D. et al., 2018, PASP, 130, 064502
Valenti J. A., Piskunov N., 1996, A&AS, 118, 595
Van Der Walt S., Colbert S. C., Varoquaux G., 2011, Comput. Sci. Eng., 13, 22
Van Eylen V., Agentoft C., Lundkvist M. S., Kjeldsen H., Owen J. E., Fulton B. J., Petigura E., Snellen I., 2018, MNRAS, 479, 4786
West R. G. et al., 2019, MNRAS, 486, 5094
Zechmeister M., Kürster M., 2009, A&A, 496, 577
Zechmeister M. et al., 2018, A&A, 609, A12
Zeng L. et al., 2019, Proc. Natl Acad. Sci., 116, 9723

SUPPORTING INFORMATION

Supplementary data are available at *MNRAS* online.

suppl_data

Please note: Oxford University Press is not responsible for the content or functionality of any supporting materials supplied by the authors. Any queries (other than missing material) should be directed to the corresponding author for the article.

APPENDIX A: VALIDATION OF STELLAR PARAMETERS

In addition to what has been presented in Section 3.1, as an independent validation, we also derived the main stellar parameters by applying the Spectroscopy Made Easy package (SME; Valenti & Piskunov 1996; Piskunov & Valenti 2017) to the co-added high signal-to-noise HARPS spectrum. SME uses grids of 1D LTE stellar models to iteratively calculate synthetic spectra whereby following a minimizing strategy each synthetic spectrum is compared to the normalized co-added spectrum observed data. The process is repeated by changing input parameters until we obtain a match for the line profiles of individual diagnostic lines, leading to values for $T_{\rm eff}$, log g, metallicity,vidual diagnostic lines, leading to values for and $v \sin i$. The turbulent velocities are calculated according to the empirical relations of Bruntt et al. (2010) and Doyle et al. (2014) and are held fixed in the determination of the other parameters. We refer to Fridlund et al. (2020) for more details and references. With this, we found a slightly cooler $T_{\rm eff} = 5182 \pm 45$ K, while the rest of the calculated values log $g = 4.25 \pm 0.07$, Fe/H $= -0.2 \pm 0.07$, $v \sin i = 2.9 \pm 0.35$ km s^{-1}, $V_{\rm mic} = 0.85 \pm 0.1$ km s^{-1} (fixed), and $V_{\rm mac} = 0.9 \pm 0.4$ km s^{-1}, are in good agreement with the respective results of Section 3.1 presented in Table 3. Finally, the result of the independent SED fitting of TOI-220 described in Section 3.3.1 is shown in Fig. A1.

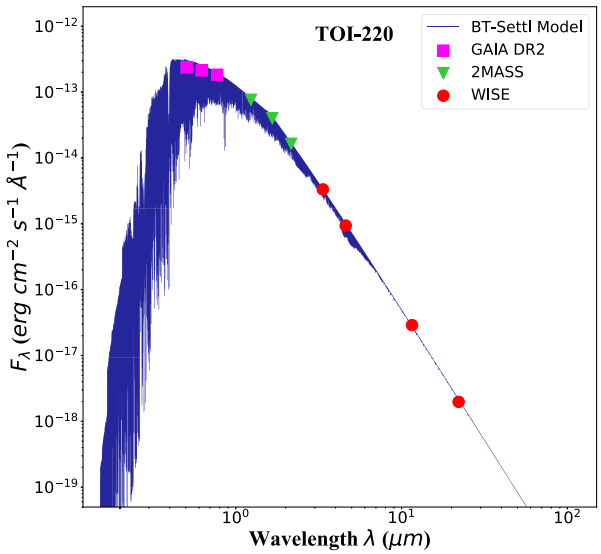

Figure A1. Independent SED fitting of TOI-220 using *Gaia* (magenta squares), 2MASS (green triangles), and *WISE* magnitudes (red circles). The blue solid line represents the fitted theoretical stellar model. See Section 3.3 for details.

APPENDIX B: PRIORS OF THE BAYESIAN ANALYSIS

In Table B1, we present the list of the prior distributions used for each parameter fitted with PASTIS code in Section 3.3.

Table B1. List of the prior distributions used in PASTIS analysis: $\mathcal{N}(\mu, \sigma^2)$: Normal with mean μ and width σ; $\mathcal{U}(a, b)$: Uniform dist. between a and b; $\mathcal{T}(\mu, \sigma^2, a, b)$: Truncated normal distribution with mean μ, width σ between a and b; and $\mathcal{S}(a, b)$: Sine dist. between a and b. (∗): parameters included in the RV drift modelling.

Stellar parameters	Distribution
Effective temperature, $T_{\rm eff}$ (K)	$\mathcal{N}(5300, 100)$
Surface gravity, log g (cgs)	$\mathcal{N}(4.5, 0.1)$
Metallicity, [M/H] (dex)	$\mathcal{N}(-0.2, 0.05)$
Distance, d (pc)	$\mathcal{N}(90.54, 5)$
$E(B-V)$ (mag)	$\mathcal{U}(0, 1)$
Systemic RV, v_0 (km s $^{-1}$)	$\mathcal{U}(20, 30)$
Reference time RV [BJD_TDB] (∗)	2458450
RV drift lin. coeff. (m s^{-1} d^{-1}) (∗)	$\mathcal{U}(-50, 50)$
RV drift quad. coeff. (m s^{-1} d^{-2}) (∗)	$\mathcal{U}(-50, 50)$
Planetary parameters	
Orbital period, P (d)	$\mathcal{N}(10.6, 0.5)$
Reference transit time, T_0 [BJD_TDB]	$\mathcal{N}(2458335.9026, 0.1)$
Planet-to-star radius ratio, R_p/R_s	$\mathcal{U}(0.029, 0.04)$
RV semi-amplitude, K (m s^{-1})	$\mathcal{U}(0, 10)$
Orbital inclination, i (°)	$\mathcal{S}(85, 90)$
Orbital eccentricity, e	$\mathcal{T}(0, 0.32, 0, 1)$
Argument of periastron, ω (°)	$\mathcal{U}(0, 360)$
Instrument parameters	
TESS contamination (per cent)	$\mathcal{T}(0, 0.005, 0, 1)$
TESS jitter (ppm)	$\mathcal{U}(0.0, 0.1)$
TESS out-of-transit flux	$\mathcal{U}(0.99, 1.01)$
HARPS jitter (km s^{-1})	$\mathcal{U}(0.0, 0.1)$
SED jitter (mag)	$\mathcal{U}(0, 1)$

APPENDIX C: SEARCH FOR TRANSITS OF PLANET-C IN TESS LIGHT CURVE

As mentioned in Section 2, by the end of the writing of this paper two new sectors (27 and 28) from the second pass of *TESS* in the Southern hemisphere became available. These new data extend the photometric baseline for additional 43 d to the initial 311 d of the first sectors (after a gap of 395 d), allowing for a search of evidence of transits of additional planet in longer orbital periods. For this, we used the Box Least Squares (BLS) periodogram method over the TOI-220 full *TESS* light curve, i.e. the photometric time-series containing the data of all the available sectors. We identified and masked the transits of TOI-220 *b* at the orbital period of 10.69 d before conducting a wide search of transit-like features in a wide range of periods and durations adopting the minimum number of events in the light curve as two. It is worth mentioning that a photometric feature at BTJD∼1417 was consistently identified as the first event by the BLS method. We confirmed that this event correspond to a known systematic spike reported in the *TESS* data release notes of the sector 4. After removing it, we found no significant peaks in the BLS. All the *TESS* light curves were also visually inspected searching for individual transits but only very low SNR features were identified. Therefore, there is no significant evidence of transits of an additional planet in the *TESS* data.

APPENDIX D: STATISTICS AND RV RESIDUALS OF THE 2 FITTED MODELS

In Table D1, we reported different statistical metrics we used to compare the models analyzed in Section 3.3.2: the single planet model with and without a radial velocity drift. We show the likelihood of each model and the ΔAIC (which favours the inclusion of the RV drift) as well as the RMS of the radial velocity residuals and the Anderson–Darling test to check for the normality of the residuals. See detailed discussion in Section 3.3.2.

Table D1. Statistical comparison of the 2 models explored in this work.

Parameter	1 planet	1 planet + RV drift
log L	55474	55484
ΔAIC	15	0
RV residuals RMS (m s^{-1})	1.93	1.69
A–D test	0.580	0.294

Notes. log L: log of the model likelihood.
AIC: *Akaike* information criterion.
A–D: Anderson–Darling test, to be compared with a critical value of 0.547, corresponding to a 15 per cent significance for normality rejection.

APPENDIX E: MASS CONSTRAINTS OF A HYPOTHETICAL COMPANION BASED ON THE RV DRIFT

We note that the RV drift defined by the linear and quadratic coefficients of Table 3, which had been defined against the epoch of the first RV point (2458440.752469 BJD), can be replaced by a purely quadratic expression, given by $RV_{\rm dr} = c_2(t - T_{0,\,\rm dr})^2 + k$, where c_2 is the quadratic coefficient of Table 3, k is an offset without physical implications, and $T_{0,\,\rm dr}$ defines the 'vertex' of the parabolic function. With c_1 being the linear coefficient of the RV drift, the time of the vertex relative to the first RV-point is given by: $t_v = -c_1/(2c_2) = 127.18$ d, which results in an absolute value of $T_{0,\,\rm dr} = 2458567.933677$ BJD. This conversion permits us to describe the RV drift as a consequence of a hypothetical circular Keplerian orbit, with the drift given by

$$y = -K \cos \frac{2\pi t}{P}, \tag{E1}$$

where K, P, and t are the RV amplitude, the period, and the time relative to $T_{0,\,\rm dr}$. Considering that the second-order Taylor expansion of $y = a \cos bx$ is given by $y = a - \frac{1}{2}x^2(ab^2) + O(x^4)$, the RVs of the Keplerian orbit can be approximated to second order by:

$$y' = -K + \left[\frac{2\pi^2 K}{P^2}\right] t^2, \tag{E2}$$

where the term in brackets corresponds now to the RV-drift's quadratic coefficient of Table 3. Hence:

$$c_2 = \frac{2\pi^2 K}{P^2} = 0.000149(31)\,(\mathrm{m\,s^{-1}\,d^{-2}}). \tag{E3}$$

Table E1. Mass constraints based on the quadratic RV drift. K, $K_{\rm min}$, and $K_{\rm max}$ are the RV amplitudes corresponding to equation (E3) solved for K, with the lower and upper errors set by the errors of c_2. $M_{\rm pl}$ is the orbiting object's mass in units of Jupiter masses, based on the central K value and a stellar mass of 0.828 $M_\odot$.

P (d)	$K_{\rm min}$ (m s^{-1})	K (m s^{-1})	$K_{\rm max}$ (m s^{-1})	$M_{\rm pl}$ ($M_{\rm Jup}$)
750	3.36	4.25	5.13	0.17
1000	5.98	7.55	9.12	0.33
3000	53.80	67.94	82.07	4.25
10000	597.80	754.84	911.90	70.5
30000	5380.16	6793.59	8207.02	916

For a given value of P, we may now solve this for K, and – using the stellar mass indicated in Table 3 – derive the mass of the hypothetical orbiter. This leads to the mass limits shown in Table E1. A lower limit of 750 d has been set, which is given by the validity of the Taylor approximation, which gets worse for shorter orbital periods. We note that only periods of less than ≈10000 d or 30 yr lead to realistic masses, since longer periods correspond to stellar mass components that would have been detected by other means; e.g. through the SED of the target.

APPENDIX F: TIMING ANALYSIS OF TOI-220 *b*

In Table F1, we reported the fitted transit time for each of the transits analysed in Section 3.4. The transit ID is the same used in Table 2. The results of the two LCO transits (Fig. F1) are also shown. We reported the difference between these transit times and the estimated TOI-220 *b* ephemeris equation (equation 1) which are presented in Fig. 8.

Table F1. Transit mid-times obtained from individual fitting and their respective timing residuals (Section 3.4) using $P = 10.695264(87)$ d and $T_0 = 2458335.9021(14)$ [BJD_TBD] (Section 3.3.2).

Transit ID	T_C [BJD_TBD]	$+\sigma$	$-\sigma$	O−C (min)
S01a	2458335.8997	0.0052	0.0083	− 3.46
S01b	2458346.5996	0.0089	0.0089	3.22
S02a	2458357.2865	0.0054	0.0054	− 8.82
S02b	2458378.6835	0.0057	0.0100	0.50
S04a	2458421.4632	0.0034	0.0034	− 1.46
S04b	2458432.1539	0.0076	0.0076	− 8.03
S05a	2458442.8599	0.0040	0.0040	7.43
S05b	2458453.5537	0.0041	0.0041	5.32
S06a	2458474.9390	0.0042	0.0042	− 2.21
S06b	2458485.6384	0.0058	0.0058	3.75
S07a	2458496.3270	0.0041	0.0041	− 5.85
S07b	2458507.0268	0.0049	0.0049	0.69
S08	2458528.4135	0.0031	0.0031	− 4.83
S09	2458549.8031	0.0051	0.0051	− 6.16
S10	2458592.5848	0.0066	0.0046	− 5.24
S12a	2458635.3685	0.0028	0.0028	− 1.43
S12b	2458646.0667	0.0052	0.0052	2.80
LCO1	2458528.420	0.024	0.024	4.53
LCO2	2458838.5808	0.0042	0.0042	1.86
S27a	2459041.7915	0.0037	0.0037	2.85
S27b	2459052.4835	0.0041	0.0041	− 1.86
S28a	2459063.1839	0.0033	0.0033	5.54
S28b	2459084.5670	0.0093	0.0093	− 5.16

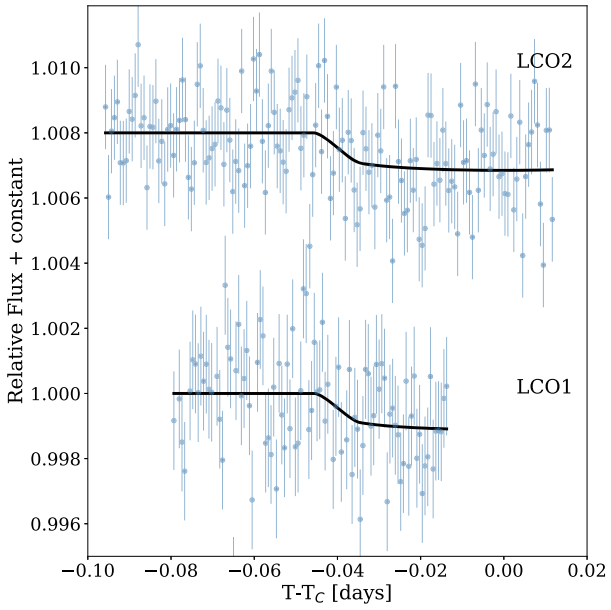

Figure F1. Two transits of TOI-220 *b* obtained with telescopes of the LCOGT network. The solid curves correspond to the fitted model of the timing analysis of the system (Sect 3.4) and are labelled with the corresponding ID of Table F1.

APPENDIX G: RADIAL VELOCITY DATA

In Tables G1 and G2, we report the radial velocity measurements together with the stellar activity indicators used in these work derived from the HARPS DRS and SERVAL, respectively (see Section 2.2).

Table G1. HARPS DRS radial velocity measurements and activity indicators of TOI-220. Exposure time and signal-to-noise ratio per pixel at 550 nm are given in the last two columns.

BJD_TDB (d)	RV ($km\,s^{-1}$)	σ_{RV} ($km\,s^{-1}$)	BIS ($km\,s^{-1}$)	FWHM ($km\,s^{-1}$)	CCF CONTRAST	$\log R'_{HK}$	$\sigma_{\log R'_{HK}}$	EXPTIME (s)	SNR (550 nm) per pixel
2458440.708866	26.4650	0.0010	−0.0273	6.1504	40.3215	−5.0453	0.0102	1800	74.8
2458440.800232	26.4658	0.0010	−0.0233	6.1550	40.3239	−5.0352	0.0114	1800	73.4
2458441.758120	26.4637	0.0010	−0.0211	6.1550	40.2942	−5.0432	0.0111	1800	73.8
2458441.778259	26.4620	0.0009	−0.0253	6.1559	40.2737	−5.0481	0.0080	1800	83.0
2458442.807269	26.4601	0.0009	−0.0254	6.1487	40.3025	−5.0262	0.0104	1800	80.2
2458442.828449	26.4621	0.0010	−0.0260	6.1543	40.3186	−5.0557	0.0122	1800	79.9
2458443.686568	26.4573	0.0009	−0.0256	6.1541	40.2811	−5.0555	0.0101	1800	78.1
2458443.775781	26.4572	0.0010	−0.0267	6.1510	40.2879	−5.0614	0.0119	1800	71.4
2458444.809444	26.4567	0.0015	−0.0265	6.1551	40.2335	−5.0456	0.0181	1800	50.3
2458446.782081	26.4577	0.0008	−0.0211	6.1489	40.2909	−5.0626	0.0092	1800	90.4
2458446.830311	26.4568	0.0009	−0.0252	6.1547	40.2613	−5.0637	0.0111	1800	89.9
2458447.738845	26.4586	0.0008	−0.0237	6.1512	40.2769	−5.0318	0.0082	1800	87.4
2458447.834355	26.4585	0.0009	−0.0277	6.1535	40.2766	−5.0801	0.0114	1800	81.7
2458451.730670	26.4629	0.0008	−0.0270	6.1515	40.3034	−5.0619	0.0086	1800	92.5
2458451.805994	26.4611	0.0009	−0.0250	6.1557	40.2822	−5.0528	0.0118	1800	83.3
2458452.702375	26.4586	0.0008	−0.0249	6.1487	40.3235	−5.0401	0.0081	1500	88.2
2458452.782399	26.4587	0.0008	−0.0268	6.1491	40.3037	−5.0383	0.0098	1800	90.7
2458453.631164	26.4596	0.0009	−0.0255	6.1596	40.2811	−5.0500	0.0090	1800	83.5
2458453.773665	26.4572	0.0009	−0.0216	6.1523	40.3094	−5.0261	0.0093	1500	83.5
2458454.627488	26.4527	0.0012	−0.0228	6.1487	40.3376	−5.0787	0.0169	1500	61.2
2458454.750359	26.4528	0.0014	−0.0269	6.1542	40.2969	−5.0989	0.0200	1800	53.3
2458455.673973	26.4538	0.0012	−0.0219	6.1500	40.3438	−5.0740	0.0158	1500	60.4
2458455.790907	26.4516	0.0012	−0.0247	6.1566	40.3110	−5.0154	0.0146	1800	62.2
2458467.755644	26.4523	0.0009	−0.0251	6.1536	40.3024	−5.0391	0.0109	1500	80.6
2458468.701619	26.4530	0.0010	−0.0242	6.1563	40.3013	−5.0400	0.0101	1500	76.3
2458469.796343	26.4550	0.0012	−0.0271	6.1548	40.2970	−5.0806	0.0184	1500	65.4
2458471.743546	26.4612	0.0011	−0.0286	6.1537	40.3077	−5.0479	0.0144	1500	69.9
2458473.769591	26.4618	0.0008	−0.0210	6.1545	40.2550	−5.0396	0.0090	1800	91.0
2458473.790575	26.4602	0.0008	−0.0206	6.1549	40.2674	−5.0433	0.0103	1800	90.8
2458475.700867	26.4556	0.0010	−0.0263	6.1564	40.2620	−5.0359	0.0112	1500	75.3
2458477.683346	26.4526	0.0010	−0.0214	6.1553	40.2887	−5.0420	0.0107	1800	78.4
2458478.764436	26.4519	0.0010	−0.0224	6.1545	40.2691	−5.0313	0.0123	1800	81.5
2458479.671230	26.4565	0.0011	−0.0252	6.1502	40.2764	−5.0191	0.0115	1800	66.7
2458480.721428	26.4585	0.0008	−0.0259	6.1560	40.2723	−5.0374	0.0088	1800	90.2
2458484.774635	26.4585	0.0010	−0.0226	6.1556	40.2878	−4.9952	0.0122	1500	74.8
2458486.707656	26.4512	0.0015	−0.0257	6.1485	40.3665	−5.0866	0.0265	1500	52.9
2458487.719322	26.4529	0.0011	−0.0192	6.1580	40.2910	−5.0331	0.0144	1500	69.9
2458488.654032	26.4539	0.0012	−0.0229	6.1566	40.3144	−5.0545	0.0145	1500	60.1
2458488.794703	26.4516	0.0012	−0.0229	6.1561	40.3274	−5.0834	0.0222	1500	68.0
2458489.695779	26.4506	0.0025	−0.0164	6.1595	40.3359	−5.1050	0.0572	1500	34.6
2458489.817157	26.4522	0.0024	−0.0165	6.1478	40.3351	−5.2218	0.0715	1500	36.1
2458490.775790	26.4522	0.0014	−0.0237	6.1567	40.3240	−5.1718	0.0303	1500	58.0
2458491.667815	26.4571	0.0013	−0.0252	6.1522	40.2983	−4.9942	0.0147	1500	60.4
2458491.787386	26.4577	0.0017	−0.0199	6.1502	40.2760	−5.0854	0.0313	1500	48.0
2458501.597810	26.4573	0.0013	−0.0258	6.1493	40.2993	−5.0926	0.0183	1500	56.1
2458501.714141	26.4537	0.0014	−0.0271	6.1552	40.2865	−5.0426	0.0208	1500	54.5
2458502.585805	26.4593	0.0011	−0.0274	6.1552	40.2717	−5.0338	0.0130	1500	65.8
2458502.714208	26.4582	0.0011	−0.0206	6.1536	40.3083	−5.0889	0.0159	1500	73.2
2458504.675128	26.4600	0.0012	−0.0258	6.1602	40.2833	−5.0751	0.0170	1500	65.3
2458505.654443	26.4601	0.0010	−0.0212	6.1560	40.2635	−5.0220	0.0109	1500	72.6
2458506.564996	26.4558	0.0009	−0.0261	6.1547	40.2964	−5.0245	0.0083	1500	83.5
2458506.726419	26.4538	0.0011	−0.0222	6.1567	40.2421	−5.1025	0.0181	1500	75.1
2458507.570571	26.4557	0.0014	−0.0259	6.1586	40.3063	−5.0686	0.0203	1500	55.0
2458507.729911	26.4560	0.0014	−0.0248	6.1560	40.2585	−5.1037	0.0263	1500	58.5
2458508.653091	26.4533	0.0015	−0.0202	6.1525	40.3208	−5.0814	0.0274	1800	54.4
2458508.673450	26.4530	0.0015	−0.0162	6.1554	40.2769	−5.0783	0.0275	1800	55.3
2458514.784388	26.4608	0.0012	−0.0229	6.1629	40.2459	−5.0436	0.0185	1800	69.8
2458515.753041	26.4586	0.0016	−0.0213	6.1576	40.2386	−5.0440	0.0302	1240	50.8
2458516.577968	26.4592	0.0010	−0.0270	6.1551	40.3106	−5.0600	0.0126	1500	79.0
2458516.748836	26.4584	0.0015	−0.0263	6.1649	40.2796	−5.1390	0.0314	1500	55.9

Table G1 – *continued*

BJD_TDB (d)	RV ($km\,s^{-1}$)	σ_{RV} ($km\,s^{-1}$)	BIS ($km\,s^{-1}$)	FWHM ($km\,s^{-1}$)	CCF CONTRAST	log R'_{HK}	$\sigma_{\log R'_{HK}}$	EXPTIME (s)	SNR (550 nm) per pixel
2458517.578103	26.4552	0.0011	− 0.0230	6.1566	40.3041	− 5.0307	0.0140	1500	69.1
2458519.545756	26.4548	0.0015	− 0.0236	6.1538	40.3182	− 5.0835	0.0255	1500	52.5
2458519.730269	26.4523	0.0029	− 0.0186	6.1508	40.2656	− 5.2730	0.1117	1500	31.6
2458520.745206	26.4550	0.0021	− 0.0245	6.1680	40.2821	− 5.1150	0.0508	1500	41.5
2458521.549624	26.4544	0.0013	− 0.0215	6.1534	40.3222	− 5.0607	0.0192	1500	59.9
2458522.730498	26.4573	0.0016	− 0.0215	6.1522	40.3176	− 5.1530	0.0509	1500	55.9
2458524.738624	26.4591	0.0012	− 0.0232	6.1538	40.3246	− 5.0988	0.0283	1500	69.5
2458528.634749	26.4563	0.0015	− 0.0292	6.1511	40.3093	− 5.1221	0.0343	1500	53.7
2458529.725206	26.4513	0.0017	− 0.0294	6.1658	40.1514	− 4.9232	0.0266	1500	51.2
2458530.732839	26.4519	0.0016	− 0.0271	6.1521	40.3033	− 5.2255	0.0526	1500	54.9
2458531.549651	26.4538	0.0009	− 0.0238	6.1536	40.3071	− 5.0648	0.0120	1800	80.7
2458535.589291	26.4626	0.0010	− 0.0252	6.1534	40.2066	− 4.9657	0.0097	1800	79.7
2458537.672021	26.4609	0.0010	− 0.0262	6.1585	40.2762	− 5.0910	0.0222	1800	82.0
2458538.689271	26.4560	0.0013	− 0.0312	6.1611	40.2935	− 5.1449	0.0319	1800	66.9
2458539.678801	26.4530	0.0011	− 0.0244	6.1564	40.2975	− 5.0551	0.0220	1800	76.0
2458540.700230	26.4541	0.0014	− 0.0254	6.1546	40.3270	− 5.1352	0.0364	1800	63.8
2458542.669892	26.4534	0.0011	− 0.0263	6.1511	40.3212	− 5.1218	0.0237	1800	80.4
2458543.677293	26.4538	0.0010	− 0.0270	6.1592	40.3075	− 5.1119	0.0218	1800	89.6
2458546.690397	26.4611	0.0015	− 0.0279	6.1612	40.3362	− 5.1225	0.0379	1800	57.7
2458547.561096	26.4596	0.0012	− 0.0283	6.1577	40.3057	− 5.0859	0.0208	1800	70.5
2458548.556934	26.4595	0.0015	− 0.0190	6.1614	40.2781	− 5.0799	0.0259	1800	55.3
2458549.552540	26.4565	0.0009	− 0.0240	6.1554	40.3031	− 5.0554	0.0135	1800	88.0
2458550.576618	26.4521	0.0009	− 0.0246	6.1621	40.2942	− 5.0500	0.0152	1800	88.9
2458554.664806	26.4555	0.0020	− 0.0280	6.1579	40.3187	− 5.0843	0.0476	1800	44.5
2458555.650955	26.4610	0.0011	− 0.0202	6.1623	40.3268	− 5.1202	0.0256	1800	75.4
2458562.535601	26.4532	0.0012	− 0.0251	6.1541	40.1392	− 5.0067	0.0142	1800	69.5
2458586.560780	26.4545	0.0012	− 0.0288	6.1560	40.3136	− 5.0919	0.0252	1800	72.1
2458591.490221	26.4594	0.0010	− 0.0267	6.1569	40.2479	− 5.0704	0.0163	1800	84.4
2458611.494962	26.4593	0.0015	− 0.0273	6.1592	40.2856	− 5.0685	0.0292	1800	60.8
2458728.879893	26.4661	0.0011	− 0.0235	6.1538	40.2937	− 5.0360	0.0131	1800	76.9
2458767.767044	26.4554	0.0012	− 0.0270	6.1482	40.1839	− 5.0234	0.0118	2100	65.9

Table G2. HARPS SERVAL activity indicators of TOI-220.

BJD_TDB (d)	dLW	σ_{dLW}	CRX ($m\,s^{-1}$)	σ_{CRX} ($m\,s^{-1}$)	Hα	$\sigma_{H\$\alpha\$}$	Na D	σ_{NaD}
2458440.708866	− 0.2623	1.4290	− 5.8768	11.5422	0.4656	0.0010	0.2665	0.0012
2458440.800232	− 4.9625	1.5490	6.7761	11.0373	0.4668	0.0010	0.2670	0.0012
2458441.758120	− 0.3565	1.3821	− 1.7498	10.5452	0.4678	0.0011	0.2648	0.0012
2458441.778259	1.3307	1.1907	7.7788	9.8335	0.4675	0.0010	0.2669	0.0011
2458442.807269	− 0.7192	1.3148	13.7782	9.0388	0.4691	0.0010	0.2604	0.0011
2458442.828449	− 2.5532	1.2666	20.1963	9.1391	0.4644	0.0009	0.2596	0.0011
2458443.686568	2.2460	1.3634	− 7.9982	10.3545	0.4654	0.0010	0.2678	0.0011
2458443.775781	2.9989	1.3117	− 4.4235	11.2185	0.4667	0.0011	0.2664	0.0012
2458444.809444	3.6119	2.0043	2.4141	13.7423	0.4705	0.0016	0.2609	0.0018
2458446.782081	0.0413	1.0744	0.8902	9.4182	0.4691	0.0008	0.2610	0.0010
2458446.830311	3.3628	1.2715	− 7.4150	10.0903	0.4681	0.0008	0.2610	0.0010
2458447.738845	0.6403	1.1213	0.1112	11.5124	0.4648	0.0009	0.2603	0.0010
2458447.834355	0.6680	1.4356	− 2.1942	11.0709	0.4663	0.0009	0.2604	0.0011
2458451.730670	− 0.0467	1.1565	6.0690	8.4936	0.4657	0.0008	0.2607	0.0009
2458451.805994	1.0959	1.3075	10.4416	9.3948	0.4649	0.0009	0.2611	0.0010
2458452.702375	− 4.0832	1.2065	− 13.0851	7.1234	0.4647	0.0009	0.2615	0.0010
2458452.782399	− 2.7432	1.2199	− 4.6426	6.7290	0.4642	0.0008	0.2597	0.0009
2458453.631164	− 0.7047	1.0873	− 2.9315	8.2828	0.4656	0.0009	0.2620	0.0011
2458453.773665	− 1.1784	1.1849	− 11.5157	8.6985	0.4646	0.0009	0.2622	0.0010
2458454.627488	− 6.1300	1.7282	13.0497	9.5861	0.4664	0.0012	0.2596	0.0014
2458454.750359	− 1.1140	2.5133	10.3401	13.2155	0.4679	0.0014	0.2617	0.0017
2458455.673973	− 4.3860	1.6552	0.0656	9.5256	0.4649	0.0013	0.2591	0.0015
2458455.790907	− 0.4042	1.7392	8.1142	10.3294	0.4678	0.0012	0.2686	0.0014

Table G2 – *continued*

BJD_TDB (d)	dLW	σ_{dLW}	CRX ($m\,s^{-1}$)	σ_{CRX} ($m\,s^{-1}$)	Hα	$\sigma_{H\$\alpha\$}$	Na D	σ_{NaD}
2458467.755644	0.0746	1.2988	0.2065	8.0561	0.4688	0.0009	0.2618	0.0011
2458468.701619	− 1.4562	1.3661	11.2744	9.5247	0.4670	0.0010	0.2618	0.0012
2458469.796343	− 1.7262	1.4104	− 5.0228	10.2855	0.4640	0.0011	0.2618	0.0013
2458471.743546	− 0.8041	1.4308	− 4.8355	10.5433	0.4666	0.0011	0.2586	0.0012
2458473.769591	2.2120	0.9652	− 11.8209	8.3775	0.4665	0.0008	0.2613	0.0010
2458473.790575	1.0648	1.2348	− 21.6860	8.0858	0.4656	0.0008	0.2668	0.0009
2458475.700867	4.6992	1.3896	8.9426	9.7111	0.4637	0.0010	0.2592	0.0012
2458477.683346	1.4648	1.2915	7.2851	7.8859	0.4664	0.0010	0.2667	0.0011
2458478.764436	− 0.6453	1.4899	− 4.9377	8.2332	0.4655	0.0009	0.2686	0.0011
2458479.671230	− 0.8130	1.7958	4.7311	10.6195	0.4703	0.0012	0.2661	0.0013
2458480.721428	2.7656	1.0797	− 13.2663	8.3028	0.4663	0.0008	0.2659	0.0010
2458484.774635	0.3673	1.5322	0.8046	9.6450	0.4645	0.0010	0.2612	0.0012
2458486.707656	− 3.1221	1.8534	− 14.3388	11.9351	0.4633	0.0014	0.2587	0.0017
2458487.719322	1.1626	1.6061	8.9141	9.9225	0.4673	0.0011	0.2610	0.0013
2458488.654032	− 2.4478	1.6747	5.4204	9.9891	0.4653	0.0013	0.2635	0.0015
2458488.794703	− 3.6027	1.6175	− 3.4279	8.9609	0.4658	0.0011	0.2627	0.0013
2458489.695779	− 4.0812	3.2346	8.1978	20.4807	0.4661	0.0021	0.2585	0.0027
2458489.817157	1.4793	3.1791	35.1790	16.5534	0.4573	0.0020	0.2648	0.0026
2458490.775790	− 1.9411	1.9919	7.9932	11.3483	0.4641	0.0012	0.2607	0.0015
2458491.667815	− 1.8741	1.9072	− 27.1674	10.1383	0.4719	0.0012	0.2612	0.0015
2458491.787386	− 1.3321	2.4345	− 0.3721	13.7161	0.4666	0.0015	0.2677	0.0018
2458501.597810	− 2.3896	1.7019	− 19.7716	12.1489	0.4692	0.0014	0.2673	0.0016
2458501.714141	0.0764	1.8841	− 3.7394	10.5970	0.4663	0.0014	0.2596	0.0016
2458502.585805	− 0.1945	1.7044	− 6.8271	9.7077	0.4652	0.0012	0.2662	0.0013
2458502.714208	− 1.9466	1.5951	− 1.6920	8.8068	0.4656	0.0010	0.2603	0.0012
2458504.675128	− 3.1907	1.5990	− 9.1703	10.9906	0.4645	0.0012	0.2599	0.0014
2458505.654443	1.9881	1.5946	− 6.0949	8.9858	0.4649	0.0011	0.2605	0.0012
2458506.564996	− 0.4999	1.2270	− 4.2423	8.2120	0.4657	0.0009	0.2584	0.0011
2458506.726419	2.2123	1.6614	− 19.0888	9.1581	0.4646	0.0010	0.2610	0.0012
2458507.570571	− 0.8163	2.1560	10.4649	15.1414	0.4643	0.0015	0.2610	0.0017
2458507.729911	4.2407	2.0254	− 7.7070	10.3599	0.4634	0.0013	0.2596	0.0015
2458508.653091	0.6389	1.9808	35.3264	12.6350	0.4602	0.0014	0.2590	0.0017
2458508.673450	1.6420	1.9984	22.2776	14.2334	0.4580	0.0014	0.2585	0.0016
2458514.784388	7.0675	1.4771	− 0.6879	10.9105	0.4560	0.0010	0.2667	0.0013
2458515.753041	8.4969	2.3699	− 13.9389	13.3166	0.4573	0.0015	0.2661	0.0018
2458516.577968	− 2.3914	1.5421	− 24.5056	9.4269	0.4591	0.0010	0.2653	0.0011
2458516.748836	3.8234	2.0109	− 4.3809	12.7091	0.4593	0.0014	0.2638	0.0016
2458517.578103	− 2.6623	1.2879	− 18.1996	9.1335	0.4581	0.0011	0.2682	0.0013
2458519.545756	− 2.7058	1.7916	− 0.4067	11.4625	0.4669	0.0015	0.2652	0.0017
2458519.730269	2.1747	4.0675	− 18.2779	19.2282	0.4634	0.0024	0.2696	0.0031
2458520.745206	1.2080	2.5333	− 13.1655	15.8645	0.4589	0.0017	0.2636	0.0022
2458521.549624	− 0.3015	1.6485	− 5.2641	10.4197	0.4608	0.0013	0.2682	0.0015
2458522.730498	− 0.9532	2.2842	27.7059	13.1662	0.4589	0.0013	0.2598	0.0016
2458524.738624	− 1.2092	1.7960	− 10.3374	11.4734	0.4593	0.0011	0.2622	0.0013
2458528.634749	− 1.0433	1.9821	− 8.1356	10.8765	0.4671	0.0014	0.2639	0.0017
2458529.725206	5.8613	2.6058	− 5.5268	13.0208	0.4623	0.0015	0.2629	0.0018
2458530.732839	3.2712	2.0613	− 26.2329	13.9351	0.4638	0.0014	0.2629	0.0016
2458531.549651	1.3428	1.2768	− 6.5268	9.4249	0.4632	0.0010	0.2630	0.0011
2458535.589291	9.7591	1.3480	− 3.8071	8.7267	0.4649	0.0010	0.2609	0.0011
2458537.672021	1.5254	1.2464	− 3.3699	9.7638	0.4674	0.0009	0.2659	0.0011
2458538.689271	− 0.6371	1.9865	15.3358	10.8076	0.4588	0.0012	0.2667	0.0013
2458539.678801	− 0.8648	1.6380	− 8.4122	10.2376	0.4589	0.0010	0.2644	0.0012
2458540.700230	− 3.6376	1.8298	− 11.8585	11.4789	0.4622	0.0012	0.2636	0.0014
2458542.669892	− 2.4210	1.4654	6.2483	9.7577	0.4602	0.0010	0.2644	0.0011
2458543.677293	− 1.3194	1.3547	− 10.0779	10.2875	0.4590	0.0009	0.2672	0.0010
2458546.690397	− 3.4933	2.0798	− 16.0068	13.8284	0.4601	0.0013	0.2658	0.0016
2458547.561096	− 2.6385	1.7150	18.2028	12.7411	0.4627	0.0011	0.2661	0.0013
2458548.556934	− 1.0987	1.8158	6.1270	12.1296	0.4673	0.0015	0.2676	0.0017
2458549.552540	− 0.2272	1.2355	− 9.1661	8.6772	0.4652	0.0009	0.2668	0.0010
2458550.576618	− 0.8848	1.3658	− 3.7954	9.2115	0.4648	0.0009	0.2675	0.0010
2458554.664806	− 1.0631	2.8411	26.3565	16.8388	0.4660	0.0018	0.2629	0.0021
2458555.650955	− 2.6379	1.6708	− 3.0134	12.1884	0.4660	0.0010	0.2617	0.0012

Table G2 *– continued*

BJD_TDB (d)	dLW	σ_{dLW}	CRX ($m\,s^{-1}$)	σ_{CRX} ($m\,s^{-1}$)	Hα	$\sigma_{H\$\alpha\$}$	Na D	σ_{NaD}
2458562.535601	11.6500	1.7232	2.8796	8.4236	0.4655	0.0012	0.2603	0.0013
2458586.560780	− 2.4692	1.5497	1.8631	10.8953	0.4670	0.0011	0.2604	0.0012
2458591.490221	2.5875	1.5793	− 6.1143	8.8415	0.4663	0.0010	0.2578	0.0010
2458611.494962	0.6165	2.0178	− 8.6563	11.9310	0.4648	0.0013	0.2675	0.0015
2458728.879893	0.9451	1.7133	− 8.4924	10.5144	0.4646	0.0011	0.2620	0.0012
2458767.767044	10.1703	1.7910	− 0.4932	11.3817	0.4690	0.0013	0.2663	0.0014

[1]*Aix Marseille Univ, CNRS, CNES, LAM, Marseille 13388, France*
[2]*Dipartimento di Fisica, Universita degli Studi di Torino, via Pietro Giuria 1, I-10125 Torino, Italy*
[3]*Centre for Exoplanets and Habitability, University of Warwick, Gibbet Hill Road, Coventry CV4 7AL, UK*
[4]*Department of Physics, University of Warwick, Gibbet Hill Road, Coventry CV4 7AL, UK*
[5]*Departamento de Física Teórica e Experimental, Universidade Federal do Rio Grande do Norte, Campus Universitário, Natal, RN 59072-970, Brazil*
[6]*Centro de Astrobiología (CAB, CSIC-INTA), Depto. de Astrofísica, ESAC campus, E-28692 Villanueva de la Cañada (Madrid), Spain*
[7]*Instituto de Astrofísica e Ciências do Espaço, Universidade do Porto, CAUP, Rua das Estrelas, P-4150-762 Porto, Portugal*
[8]*Departamento de Física e Astronomia, Faculdade de Ciências, Universidade do Porto, Rua do Campo Alegre, P-4169-007 Porto, Portugal*
[9]*Leiden Observatory, Leiden University, NL-2333CA Leiden, the Netherlands*
[10]*Department of Space, Earth and Environment, Chalmers University of Technology, Onsala Space Observatory, SE-439 92 Onsala, Sweden*
[11]*Center for Astrophysics, Harvard and Smithsonian, 60 Garden Street, Cambridge, MA 02138, USA*
[12]*NASA Ames Research Center, Moffett Field, CA 94035, USA*
[13]*Instituto de Astrofísica de Canarias, E-38205 La Laguna, Tenerife, Spain*
[14]*Departamento de Astrofísica, Universidad de La Laguna, E-38206 La Laguna, Tenerife, Spain*
[15]*Sub-department of Astrophysics, Department of Physics, University of Oxford, Oxford OX1 3RH, UK*
[16]*George Mason University, 4400 University Drive, Fairfax, VA 22030, USA*
[17]*International Center for Advanced Studies (ICAS) and ICIFI (CONICET), ECyT-UNSAM, Campus Miguelete, 25 de Mayo y Francia, (1650) Buenos Aires, Argentina*
[18]*Thüringer Landessternwarte Tautenburg, Sternwarte 5, D-07778 Tautenburg, Germany*
[19]*NASA Exoplanet Science Institute, Caltech/IPAC, Mail Code 100-22, 1200 E. California Blvd., Pasadena, CA 91125, USA*
[20]*Department of Physics and Astronomy, Swarthmore College, Swarthmore, PA 19081, USA*
[21]*U.S. Naval Observatory, 3450 Massachusetts Avenue NW, Washington, DC 20392, USA*
[22]*Observatoire de l'Université de Genève, Chemin des Maillettes 51, CH-1290 Versoix, Switzerland*
[23]*University of Zürich, Institute for Computational Science, Winterthurerstrasse 190, CH-8057 Zürich, Switzerland*
[24]*European Southern Observatory, Alonso de Cordova 3107, Vitacura, Santiago, Chile*
[25]*Department of Physics and Kavli Institute for Astrophysics and Space Research, Massachusetts Institute of Technology, Cambridge, MA 02139, USA*
[26]*Department of Earth, Atmospheric and Planetary Sciences, Massachusetts Institute of Technology, Cambridge, MA 02139, USA*
[27]*Department of Aeronautics and Astronautics, MIT, 77 Massachusetts Avenue, Cambridge, MA 02139, USA*
[28]*Hazelwood Observatory, Churchill Victoria, 3842, Australia*
[29]*Mullard Space Science Laboratory, University College London, Holmbury St. Mary, Dorking, Surrey RH5 6NT, UK*
[30]*Department of Astrophysical Sciences, Princeton University, 4 Ivy Lane, Princeton, NJ 08544, USA*
[31]*Univ. Grenoble Alpes, CNRS, IPAG, F-38000 Grenoble, France*
[32]*Astrophysics Science Division, NASA Goddard Space Flight Center, Greenbelt, MD 20771, USA*
[33]*Deutsches Zentrum für Luft- und Raumfahrt, Institut für Planetenforschung, D-12489 Berlin, Rutherfordstrasse 2., Germany*
[34]*Center for Planetary Systems Habitability and McDonald Observatory, The University of Texas at Austin, Austin, TX 78730, USA*
[35]*Noqsi Aerospace Ltd., 15 Blanchard Avenue, Billerica, MA 01821, USA*
[36]*Rheinisches Institut für Umweltforschung an der Universität zu Köln, Aachener Strasse 209, D-50931 Köln, Germany*
[37]*Astronomical Institute of the Czech Academy of Sciences, Fričova 298, CZ-25168 Ondřejov, Czech Republic*
[38]*Stellar Astrophysics Centre, Department of Physics and Astronomy, Aarhus University, Ny Munkegade 120, DK-8000 Aarhus C, Denmark*
[39]*Department of Astronomy, University of Tokyo, 7-3-1 Hongo, Bunkyo-ku, Tokyo 113-0033, Japan*
[40]*Space Telescope Science Institute, 3700 San Martin Drive, Baltimore, MD, 21218, USA*
[41]*NCCR/PlanetS, Centre for Space and Habitability, University of Bern, Gesellschaftsstrasse 6 (G6), CH-3012, Bern, Switzerland*
[42]*Astronomy Department and Van Vleck Observatory, Wesleyan University, Middletown, CT 06459, USA*
[43]*SETI Institute, Mountain View, CA 94043, USA*
[44]*Department of Astronomy, Columbia University, 550 W 120th Street, New York, NY 10027, USA*

This paper has been typeset from a TEX/LATEX file prepared by the author.